Development of an Advanced Materials System for Tooling Produced by Three-Dimensional Printing

by

Zubin Jamshed Irani

B.Tech. Materials and Metallurgical Engineering
Indian Institute of Technology, Kanpur, India, 1996

Submitted to the Department of Materials Science and Engineering in Partial Fulfillment of the Requirements for the Degree of

MASTER OF SCIENCE IN MATERIALS SCIENCE AND ENGINEERING

at the

Massachusetts Institute of Technology

February, 1999

Signature of Author _____
Department of Materials Science and Engineering
January 15,1999

Certified by _____
Samuel M.Allen
Professor of Physical Metallurgy
Thesis Supervisor

Accepted by _____
Linn W. Hobbs
John F. Elliott Professor of Materials
Chairman, Departmental Committee on Graduate Students

Development of an Advanced Materials System for Tooling Produced by Three Dimensional Printing

by

Zubin Jamshed Irani

Submitted to the Department of Materials Science and Engineering
on January 15, 1999 in Partial Fulfillment of the Requirements for the
Degree of Master of Science in Materials Science and Engineering.

Abstract

Three Dimensional Printing (3DP™) is a manufacturing technique in which a powdered material is used to build parts with complicated geometries directly from a three dimensional computer model. This technique has been used in the past to manufacture metal parts with complicated geometries. The three different materials used in the making of tools by 3DP™ are binder, metal powder and the low melting infiltrant. The original material system used for hard tools is 420 martensitic stainless steel powder, a Cu-10Sn alloy as the infiltrant and acrysol as the binder. Although almost 50 tools have been manufactured using this materials system, there were several concerns which had to be dealt with, including dimensional control, porosity control, erosion and interaction between the skeleton and the infiltrant. Another requirement is a "hardenable" material system that is soft initially and that can be hardened after machining. This thesis describes the development of a new hardenable material system in which most of the concerns with the 420/bronze system are eliminated.

The new material system that was selected uses a Mo powder skeleton and a 56Cu-22Ni-22Mn infiltrant. The Cu-Ni-Mn alloy is age hardenable. Acrysol was retained as the binder material again. Experiments were carried out to study the printing, debinding/sintering and infiltration steps. An extra age hardening step was also introduced after infiltration. The process parameters for each of the steps were developed and several tools have been manufactured successfully. The thesis describes each of the post processing steps in detail with regards to experiments that were performed or literature that was obtained from past work. The tools that were manufactured with the new material system showed better properties on the whole than those manufactured with the previous material system.

Thesis Supervisor: Samuel M. Allen
Title: Professor of Physical Metallurgy

Acknowledgements

I would like to thank the DARPA/NSF TRP Program on Low-Cost, High Performance Tooling and the members of the Three Dimensional Printing Industrial Consortium for their support. I would also like to thank the following people:

Sam Allen, for his support and guidance all the way through. I could not have asked for a more supportive advisor. It was a pleasure working with you.

Ely Sachs, for the constant guidance and direction that played a very crucial role in my work.

Jim Serdy, one of the coolest and most patient people I have ever met. Thank you for printing all my stuff and all those interesting conversations.

Dave Brancazio, for always being able to answer my questions and helping me out on numerous occasions.

Chris, for being a great friend and group-mate. Thank you for helping me out with the initial work on the 420/bronze system.

Calvin, for helping me out with the work on coatings.

Costas, thank you for accompanying me during the journey in search of a test to measure accurately low shrinkages.

Adam and Ram for helping me use "The furnace", the only one which could age harden my parts.

John Centorino for helping me out with the MRF furnaces.

All other students in the 3DP lab, for all you help. Best of luck in the future.

India-Club: Phalee, Sawan, John, Praveen and Sri for cheering me up when the chips were down, supplying computers, paper, and wisdom.

I would like to especially thank Phalee for making my time at MIT an unbelievable experience.

My DMSE friends : Chris & Julliane, Jim, Richard, Wendy and Mike.

Lastly but not the least my family for giving me the genes, being my support and making sure that all is well at home.

Table of Contents

List of Figures

List of Tables

1 Introduction

The manufacturing industry has faced a number of changes over the past few years. Many plants have had to focus on new issues in order to remain competitive. Productivity has given way to quality which has given way to customer satisfaction. Customers have become much more demanding today and many firms find that in order to meet customer demand they have to increase their product mix, constantly update the product design and reduce the lead time from design to manufacturing. At the same time, in order to remain competitive, they have to maintain quality and reduce costs. In such an environment rapid prototyping or rapid manufacturing techniques play a very important role.

1.1 Three dimensional printing (3DP^{TM})

Three-dimensional printing (3DP^{TM}) is a rapid prototyping technique. It was invented at MIT, [1] and is illustrated in Fig. 1-1. Using this technology a prototype or physical object is built from its computer-aided design (CAD) file. The CAD model of the object is sectioned into layers using a slicing algorithm. A layer of powder is first spread on a substrate. Binder material is deposited into the layer following a computer pattern that is

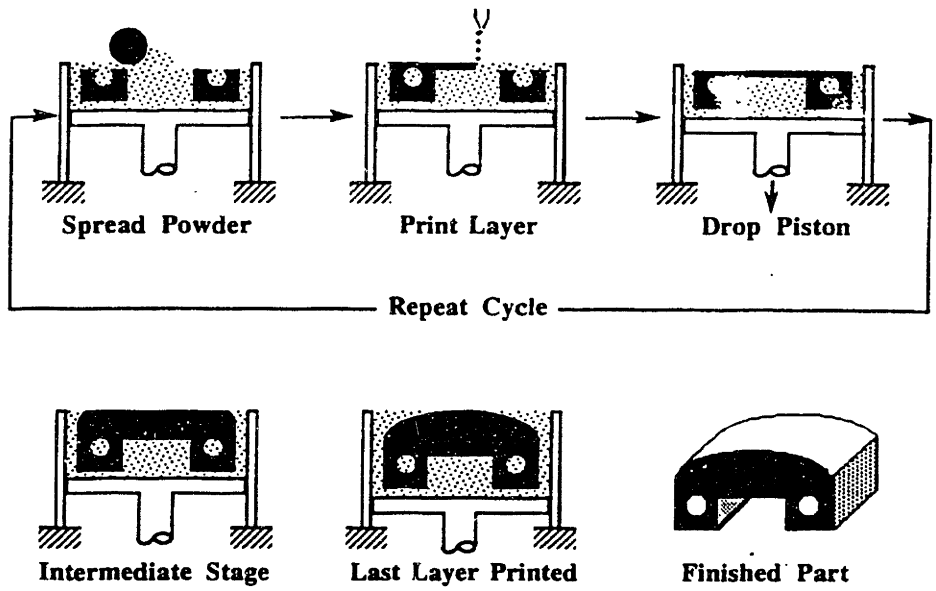

Figure 1-1 : The Three Dimensional Printing process for metal tooling (3DP^{TM})

generated from each slice. The binder material is deposited using a using a print head similar to that in an ink-jet printer. After the printing of a single layer is complete, the substrate is lowered and a new layer is spread on top of the previous one. After this layer is selectively joined another powder layer is spread on it, and so on. This process is repeated until all the layers are printed. The loose powder is brushed away leaving a 3D skeleton of powder glued together with the binder. This is commonly referred to as the "green part". A monomodal spherical powder skeleton occupies 60% of the volume of the part. The other 40% is comprised of the binder and the porosity.

Three Dimensional Printing shows tremendous potential for parts with complex geometries and short lead-time requirements. It is one of the few rapid prototyping technologies that can fabricate conformal cooling channels and truss structures. These features involve very complex geometries and cannot be achieved through the standard manufacturing techniques.

1.2 Applications of 3DP to metal injection molding tooling

Product designs change very rapidly in several manufacturing industries, however it takes a lot longer before manufacturing commences. The bottleneck in the change process is often the fabrication of molds or dies for injection molding. It takes weeks and sometimes even months to manufacture a mold with standard manufacturing techniques. Any cycle-time reduction in the mold manufacturing process would generate significant returns. 3DP™ can be used to fabricate the same molds in a few days.

Three Dimensional Printing (3DP™) has been successfully applied to the fabrication of injection molding tooling using metal powders. The ability to manufacture tooling with a complex geometry quickly and at low cost, makes 3DP™ a very appealing alternative to standard manufacturing techniques. To date, more than 50 tools have been manufactured and used to mold plastic parts. 3DP™ allows incorporation of features in the parts which are impossible to manufacture via other standard manufacturing techniques. One such feature is a cooling channel that conforms closely to the working surface of the tool [2].

Conformal cooling channels have been shown to reduce distortion in the plastic parts along with a 15% reduction in the cycle time [3]. Hence the injection molding tooling market looks very promising for the 3DP™ technology.

The process of fabrication of an injection mold via 3DP™ comprises of the printing operation followed by a post processing treatment. The post-processing (Fig. 1-2) comprises debinding/reduction, sintering and infiltration to full density. The material system for an injection mold has three components or dissimilar materials. They are the (1) binder, (2) metal powder and (3) low melting infiltrant.

1.3 Criteria for materials selection in 3DP tools

The binder is used to selectively join the powder particles together during printing. There are many requirements for this binder material [4]: (1) it should provide reasonable green strength to the skeleton; (2) it should be able to be charged electrostatically; (3) it should flow through a jet nozzle easily; (4) it should not affect the shrinkage behavior during sintering; (5) it cannot be corrosive to the skeleton, furnace or printing machine; and (6) it should wet the skeleton very well. Acrysol is used currently as the binder for printing with 420/316L stainless steel powders.

The metal powder forms the skeletal structure and occupies 60% of the volume of the part. The powder should spread very easily into layers in order to achieve a high printing density. Hence, spherical powder is preferred. The size distribution of the powder must be uniform and its sintering behavior should be uniform and predictable. The powder should also have a low solubility in the infiltrant at high temperatures. The powders initially used for 3DP™ tooling were 316L and 420 stainless steel [5].

A low melting alloy is used to infiltrate the sintered part to full density. A capillary force drives the infiltrant into the voids between the powder particles. This requires that the melting point of the infiltrant be lower than that of the skeleton and that the wetting of the powder be good. Another important requirement is that the solubility of the skeleton in

the infiltrant be very low at high temperature. The infiltrant being used in the original system was Cu-10 wt.% Sn or commonly known as "10% tin bronze".

1.4 Post-processing of the 3DP™ metal tool

The post processing of the 3DP™ tool has three main steps: (1) debinding/reduction, (2) sintering and (3) infiltration. These are illustrated in Figure 1-2. The debinding step is carried out to evaporate the binder material and leave behind a very lightly sintered skeleton. The part is held at a temperature of 200 °C and 500 °C for a small period of time. The heating rate is very critical and should not exceed 5 °C/min in order to prevent the formation of large blow holes due to the escaping binder gases. The sintering process is next and it gives the skeleton the required strength for the infiltration process. The skeleton is held at a temperature of at least half the melting point of the skeleton material for a period of time.

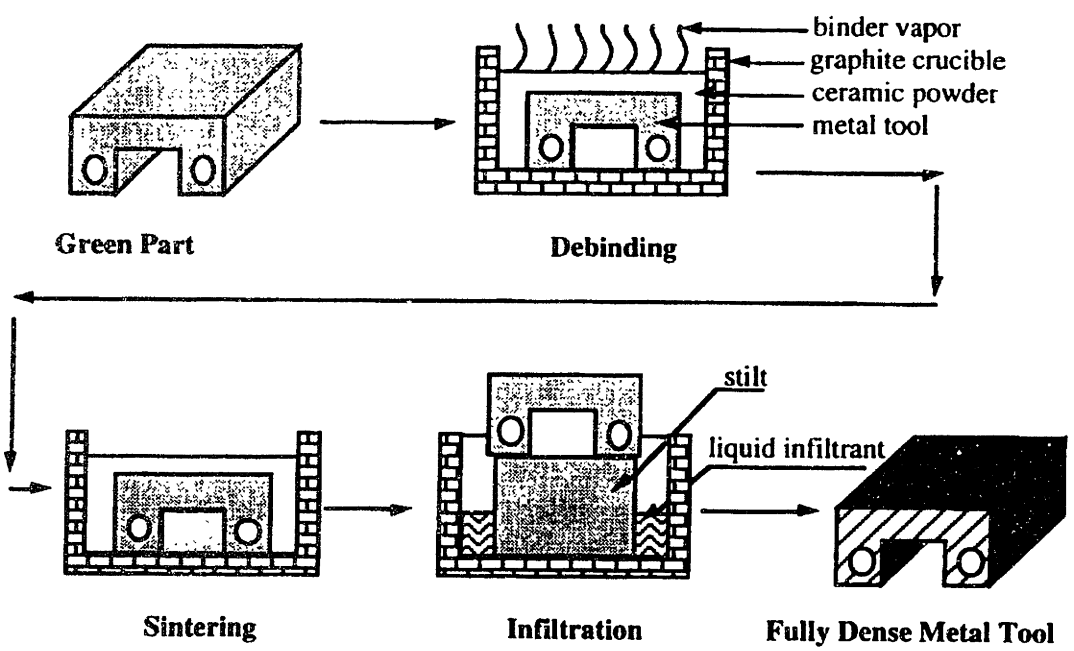

Figure 1-2 : The Post Processing Cycle for the 420/Cu-10Sn metal tool.

However, excessive sintering causes more shrinkage. The optimum degree of sintering is a very delicate tradeoff between the strength required and the amount of shrinkage that can be tolerated. The infiltration is the last step and it is done to fully densify the part. The skeleton and the infiltrant are heated to a temperature above the melting point of the infiltrant and below that of the skeleton. The liquid infiltrant flows into skeleton due to the capillary force, similar to a dry sponge absorbing water.

1.5 Major problems associated with the post processing of 420/bronze

There were four major problems associated with the original 420/bronze system [4]. These are dimensional error, porosity, erosion, inter-diffusion between skeleton and infiltrant and machinability. The dimensional tolerance is a very important concern in the tooling industry. A change in dimensions occurs mainly during sintering in the form of shrinkage. The porosity, erosion and interdiffusion are problems that occur during infiltration.

1.5.1 Dimensional control

The 3DP tooling application demands very strict dimensional tolerances. There are three major sources for the dimensional error. The first source is non-uniform shrinkage during sintering. The second is non-uniform expansion during infiltration and the last is distortion from heat treatment. To solve the sintering shrinkage problem correlations were developed for the 420 and 316L powders so that the percent shrinkage could be predicted as a function of the sintering temperature. This predicted shrinkage was compensated for in the printing step. There are a few drawbacks with such an approach. The first is that the correlation would have to be recalculated for any change of variables in the system, such as furnace, furnace atmosphere, supporting material and crucible material. The other drawback is the variability in shrinkage, which can be high. A better approach is to reduce absolute value of shrinkage thus simultaneously reducing its variability.

The second source of dimensional error comes from the infiltration process. For the 316L or 420/bronze systems an average expansion of ~0.35% has been observed. The reason for this behavior is not known for sure. Several hypotheses have been formulated and most of them relate to the interdiffusion between the steel particles and bronze infiltrant [4]. Therefore a potential solution to the problem would be to find a non-reacting system.

The last source of dimensional error comes from any phase transformation that the infiltrant or the skeleton undergo. In the 420/bronze system the steel particles undergo a martensitic transformation during cooling after infiltration. The cooling rate is fast enough (21 °C/min) to induce this transformation. The Cohen and Roberts model [6,7] shows that an expansion as high as 1% can occur during the martensitic transformation in a 420 steel with a carbon concentration of 0.47% (typical for our 420 powder). Other heat treatments like age hardening are less distortive and could lead to much less dimensional change.

1.5.2 Erosion control

The erosion of the skeleton in the liquid metal infiltrant is one of the major problems faced during infiltration. It occurs when elements in the skeleton are soluble in the infiltrant at the infiltration temperatures. The final state of this dissolution is the equilibrium thermodynamic state at the infiltration temperature. A high diffusivity of the skeleton elements in the liquid infiltrant makes the dissolution process kinetically feasible. Erosion can destroy the structural integrity of the part and cause slumping. In the 420/bronze system, 2-3 wt.% iron was found in the infiltrant using microprobe analysis. This would result in a significant amount of the skeleton dissolving in the infiltrant. In the case of a large part, a significant amount of the skeleton will dissolve in the infiltrant. Methods like using a stilt or pre-alloying the infiltrant have been used to solve this problem and have met with reasonable success. However it is more desirable to have a material system where the skeleton does not dissolve in the infiltrant. This would limit erosion and also prevent loss of structural integrity. An another solution would be to use a material system where the diffusivities of the constituents of the skeleton are very small.

1.5.3 Porosity control

Residual porosity is another problem that can arise during infiltration. These pores can lead to several problems. They can be the source of small micro-cracks, which cause the mechanical properties of the tool to degrade over time. However, a more serious problem has to do with continuous pores. They can cause coolant to leak from the cooling channels to the mold surface and destroy the plastic parts. The residual porosity after infiltration occurs mainly due to two reasons [8]: the infiltrant never filled the region (entrapped porosity) or because voids were formed within the infiltrant region during cooling and solidification.

Entrapped porosity tends to occur on a large scale relative to the powder size. It occurs due to surface contamination or oxidation which is detrimental to wetting. This causes the infiltrant to loose its driving force and it does not travel to those regions. In order to prevent oxidation, a reducing atmosphere can be used, i.e., hydrogen or another reducing gas. Entrapped gas may also cause an infiltrant not to reach a region in the skeleton. If the liquid infiltrant were to envelop a region with trapped gas, the gas pressure would build up as the infiltrant closed in on the region. When the gas pressure equalized with the capillary pressure driving the infiltration, infiltrant flow would stop [8]. It has been shown that the final pressure in a bubble of gas (~15 μm in size) trapped in the solid infiltrant (Cu-10Sn) is 0.5 atmosphere [8].

Porosity due to solidification of infiltrant is a very common phenomena that occurs in many castings and it can be attributed to shrinkage voids or gas porosity. Shrinkage voids occur due to a volume change when the infiltrant solidifies (~2% for bronze). The gas porosity occurs due to the fact that the solubility of hydrogen (H_2) gas is much more in liquid bronze versus solid bronze. Hence, gas pockets are formed as the excess gas is given out during the solidification of liquid bronze.

The main reason for porosity in both the above cases is the relatively slow diffusion of hydrogen gas in the liquid infiltrant. In order to speed up the diffusion, infiltration was

carried out under two different atmospheres in the same cycle [4]. The part was initially heated up to just below the melting point of bronze under a hydrogen atmosphere. The hydrogen was pumped out and the remainder of the infiltration was carried out under vacuum. Although the microstructures showed less porosity, some tools produced with this vacuum process leaked as a result of connected porosity. It was initially felt that a plausible reason for this observed phenomenon could be the wide freezing range of the Cu-10Sn alloy (~150 °C). The solidification is dendritic in these alloys and the gas porosity tends to appear along the inter-dendritic regions [9]. This could lead to connected porosity within the tool and hence leaking. However similar results were obtained after the infiltration of 420 with pure Cu (no freezing range). This disproved the earlier hypothesis. The new belief is that the connected porosity occurs due to solidification shrinkage of the infiltrant alloy.

1.5.4 Interaction control between 420 and bronze

At the infiltration temperature ~1200 °C, the diffusivities of the various elements would be high in the 420 steel and the bronze infiltrant. Hence if the reaction between the infiltrant and the powder is thermodynamically feasible then interaction cannot be avoided. The 420 stainless steel powders did react slightly with the infiltrant. In order to prevent inter-diffusion a possible solution would be to use a skeleton material with a high melting point. This would make the diffusivity of other elements in the skeleton very small.

1.5.5 Machinability

The machinability of 420/bronze is very poor and results in extensive tool wear. This primarily due to the hardened 420 powder particles in the as infiltrated part.

1.6 Development of a new material system

This thesis describes the development process of a new material system, which could eventually replace the 420/bronze system. The nature of the 3DP™ process does put many restrictions on the alloy design, as discussed in the next chapter. The goal in developing the new material system is to improve upon many limitations associated with the previous hardenable system. The new material system is a Mo powder skeleton and a Cu-Ni-Mn alloy. It is expected to show superior behavior to the 420/bronze system in many respects. The next chapter discusses the methodology for selecting the material system. Chapters 3 through 6 describe the development of the post processing for this system. Chapter 7 discusses some of the limitations that the system faces and alternative approaches that were tried in order to improve on the limitations. Chapter 8 concludes the work, emphasizing on the advantages of the Mo/Cu-Ni-Mn system versus the 420/Cu-10Sn system. It also suggest future work that could be pursued.

2 Development of a New Material System

2.1 Alloy design constraints for 3DP™ tooling

Certain mechanical properties are very important for the proper functioning of injection molding tooling, the most important being wear resistance. Wear is defined as erosion resulting from mechanical friction between the plastic part and the tool. There is also metal-to-metal wear at ejection pins and "slides". A strong correlation exists between the hardness of a material and its wear resistance. Hence, a higher hardness for the tool will lead to better wear resistance and the alloy design should take this into consideration. However, the nature of the 3DP™ process puts many restrictions on the alloy design process.

The melting point of a crystalline material like a metal or an alloy is a function of the strength of the chemical bond in the material. The bond strength also determines other properties like hardness and strength of the material. As a result of this correlation a high melting point implies a high hardness [10]. Figure 2-1 confirms this relationship for common metals and alloys. The 3DP™ process requires that the melting point of the infiltrant be lower than the skeleton. Hence, the hardness of the infiltrant will also be lower than the skeleton. It is so far been very common in a 3DP™ tool to have the hard phase as the skeleton and the softer phase as the infiltrant. In order to improve the hardness of the material system a hardenable skeleton or infiltrant or both could be used, i.e., a successive heat treatment could be given to harden the relevant phase. A hardenable phase is one which exists initially in a soft state and can be hardened later by a heat treatment.

A hardenable material system has several advantages. One big advantage is machining. The machining of a part with a lower hardness is a lot easier. Hence the tool could be machined in its unhardened condition and then subsequently hardened.

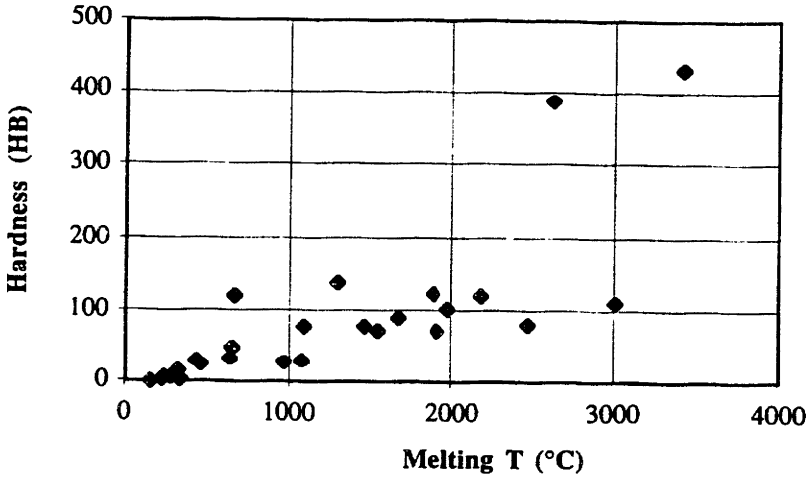

(a) Melting temperature vs. hardness for pure metals

(In,Se,Sn,Bi,Cd,Pb,Zn,Te,Sb,Mg,Al,Ag,Au,Cu,Be,Ni,Fe,Ti,Cr,V,Rh,Tc,Nb,Mo,Ta,W)

melting point increase

Figure 2-1 : Hardness versus melting point for several metals.

Another advantage of hardenable tooling is that the level of hardness could be tailored according to the application. This could be done by modifying the hardening treatment. As mentioned earlier, either the skeleton, the infiltrant or both could be hardenable. The most ideal case would be one where both the skeleton and the infiltrant are hardenable. However, there are many problems associated with such a scenario. The heat treatments for the skeleton and the infiltrant should be compatible i.e. heat treatment of one phase should not degrade the properties of the other. This is extremely difficult to achieve and hence it would be more practical to use either a hardenable skeleton or infiltrant. An additional requirement for a hardenable material system is minimum distortion during the hardening treatment.

The 420/bronze material system is an example of a hardenable skeleton. The 420 stainless steel is martensitic. During the furnace cooling after infiltration a hard martensite phase forms resulting in high overall hardness of the system. An attempt was made to assess the effects of an annealing and quenching treatment after infiltration of 420/bronze. The next section describes that effort and the results obtained.

2.2 Post-infiltration annealing and quenching of the 420/bronze system

An attempt was made to introduce two heat treatments after the infiltration of 420/bronze. The first one was an annealing treatment to soften the steel particles, in order to enable easier machining to final dimensions. After machining a quenching treatment was given to re-harden the part. A critical issue was the distortion that occurred during the quench treatment. The re-hardening of the 420/bronze is necessary in order to obtain a high hardness and wear resistance which is very critical for the proper functioning of the tool.

2.2.1 Experimental procedure

Rectangular coupons (1" x ½" x ¼") of 420/bronze were machined and the dimensions were measured accurately using calipers. Differential scanning calorimetry (DSC) was performed on the shavings of the 420/bronze composite. The results can be seen in Figure 2-2. There are two major phase transformations of interest. The first occurs at 840 °C when the ferrite phase (α) in the 420 particle transforms to the austenite phase (γ). The second transformation occurs at 900 °C when the bronze infiltrant begins to melt. Both these temperatures are very important in developing the annealing and quenching heat treatments. A theoretical study of the phase transformations occurring in 420 stainless steel was done using the "Thermocalc" thermodynamic software. The austenitizing temperature was found to be 840 °C (Figure 2-3) where the α phase transforms to the γ phase. Hence, the "Thermo-Calc" results matched those obtained from the DSC work.

The annealing treatment comprised of holding the coupons at several temperatures below 840 °C (austenitization temperature) for 3 hours. The holding time was critical because excessive grain growth could lead to a reduction in hardness and ductility of the quenched part. Suitable times were calculated taking into account the thickness of the sample [11]. The coupons were then cooled at 1 °C/min until 250 °C and then at 2 °C /min (The nose of the TTT curve for 420 steel [11] is at 250 °C). The cooling rate had to be slow enough in order to prevent any martensite formation.

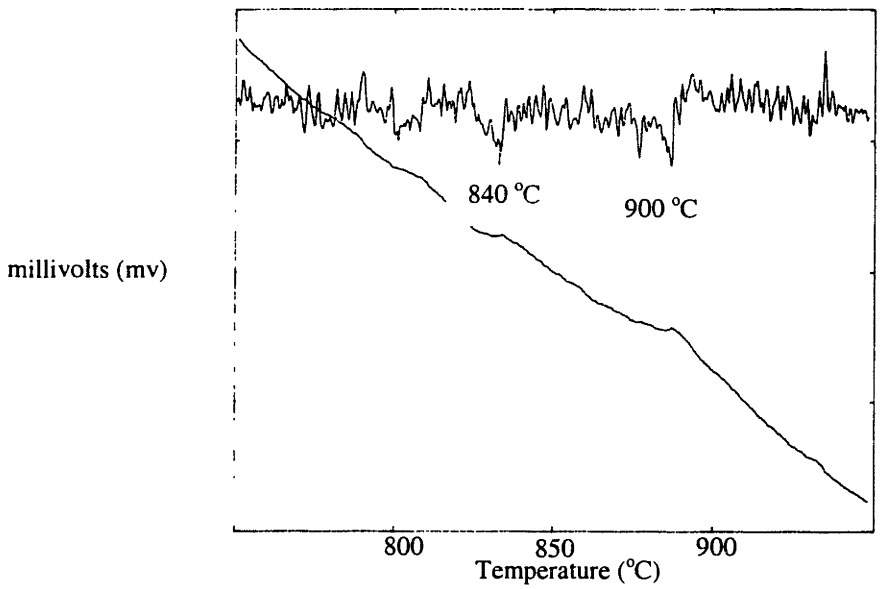

Figure 2-2 : Differential Scanning Calorimetry (DSC) for the 420/bronze system.

After annealing, the dimensional measurements were again noted using calipers. A part of the coupon was sectioned, mounted and polished. Micro-hardness readings on the 420 powder and the bronze infiltrant along with macro-hardness measurements were taken on several sections. Figure 2-4 is a micrograph of one such section. The steel particles and the Bronze infiltrant can be seen very clearly. The next step was the quenching treatment. The coupon was held at a temperature of 880 °C (above the austenitization temperature) for 1-½ hours in order to reform the austenite 'γ' phase (solution treatment). The holding time was again very critical in order to prevent excess grain growth [11]. The coupons were then furnace cooled at 20 °C/min. to room temperature. This cooling rate should be high enough to form martensite.

Dimensional and hardness tests were again performed on the quenched specimens. Measurements were also taken with a coordinate-measuring machine (CMM) to study the distortion that occurred during the quenching treatment.

All the hardness micro-hardness measurements were taken using a 100g Vickers indentor and then converted to the Rockwell C scale in reporting results.

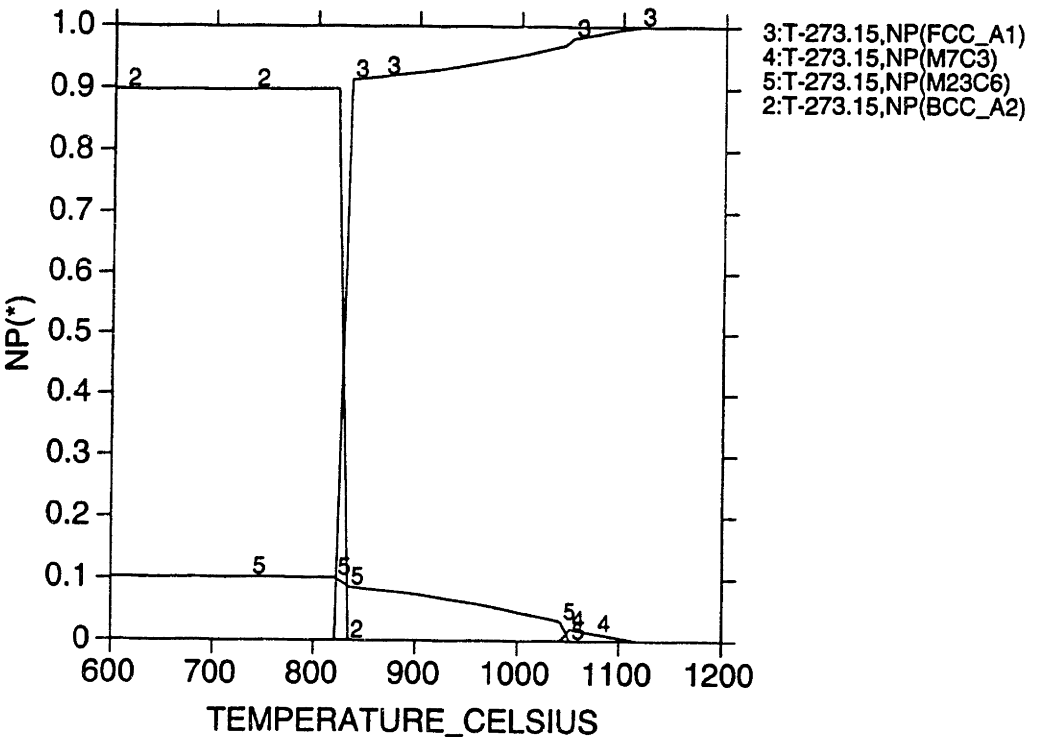

Figure 2-3 : The phase mole fraction vs. temperature plot for 420/Cu-10Sn

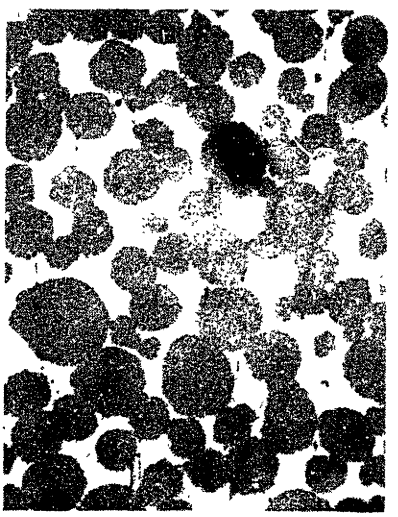

Figure 2-4 : Microstructure of the infiltrated 420/Cu-10Sn.

2.2.2 Results

The annealing treatment showed very promising results. Table 2-1 shows that the as infiltrated hardness of the 420 powder was 56 Rc (Rockwell C Scale). After annealing the hardness went down to 22 Rc. However the quenching treatment was not able to re-establish the as infiltrated hardness. The hardness obtained after the quenching treatment was only 48 Rc. The macro-hardness of the coupon dropped from 25 Rc in the as infiltrated condition to 94 Rb in the quenched condition. There could be several reasons for this behavior. The temperature window for the solution temperature before quenching is very small due to the small difference between the melting point of the infiltrant (900°C) and the α to γ transformation temperature of the steel phase (840 °C). Another potential reason could be the formation of a stable carbide phase during annealing which does not dissolve during the austenitizing (solution treatment) and reduces the hardenability of the 420 stainless steel. Table 2-2 shows the dimensional changes that were observed after the annealing and quenching steps. A total dimensional change of 0.2% expansion was observed in all the three dimensions, mainly during the annealing treatment. CMM measurements showed that the distortion during quenching was minimal and below the measuring reliability at high precision. The detailed annealing and quenching treatments are listed in Appendix 1.

	Micro-hardness		Macro-hardness
Heat Treatment	**420 Particle**	**Bronze (Cu-10Sn)**	**composite**
As infiltrated	56 Rc	80 Rb	25 Rc
Annealing	22 Rc	81 Rb	79 Rb
Quenching	48 Rc	82 Rb	94 Rb

Table 2-1 : Hardness Readings for the 420/Cu-10Sn system

Heat Treatment	%Δlength	%Δwidth	%Δthickness
Annealing	0.18	0.17	0.17
Quenching	0.01	0.003	0.06
Total	0.19	0.173	0.23

Table 2-2 : Dimensional Changes during annealing and quenching of 420/Cu-10Sn

2.2.3 Conclusion

The 420/Bronze system has limited re-hardenability due to the low melting point infiltrant and inability to re-dissolve carbides because of the very small temperature window for austenitization (between 840 °C and 900 °C). The total dimensional changes that occur during annealing and quenching are around 0.2% expansion. It is concluded that this material system is not particularly suited for re-hardening purposes. The main issues are that the 420/bronze can be annealed and re-hardened but not so successfully and it involves extra process steps/complexity.

2.3 The Mo/Cu-Ni-Mn system

The limited success with re-hardening the 420/Bronze system led to the development of a new hardenable material system. After studying several possible candidates, the Mo/Cu-Ni-Mn system was chosen. It was decided that it would be desirable to have a hard powder with a high melting point along with a hardenable infiltrant. Mo has a high melting point (~2610 ° C) and a relatively high hardness (~25 Rc). The only two other readily available metals with a higher melting point are W and Ta. Mo has been used in the past as a valuable alloying agent, contributing to hardenability and toughness of quenched and tempered steels. It also improves the strength of steel at high temperatures. The infiltrant, Cu-Ni-Mn is age hardenable i.e. it can be hardened by a heat treatment. The binder to be used was acrysol because it had been successfully used in the past.

2.3.1 Potential advantages of the Mo/Cu-Ni-Mn system

In the new material system, both the phases were expected to be hard in the final condition. The Mo particles were expected to be inherently hard and the Cu-Ni-Mn infiltrant could be hardened by a heat treatment. This is in contrast to the 420/bronze system where the 420 stainless steel particles were very hard and the bronze phase was very soft.

The second potential advantage had to do with the nature of the heat treatment required to harden the Cu-Ni-Mn infiltrant. The age hardening treatment required to harden Cu-Ni-Mn was not aggressive like the quenching treatment required to re-harden the 420 stainless steel. Hence, it was expected that it would lead to less dimensional change and distortion in the part.

The reaction between the Mo and Cu-Ni-Mn infiltrant was also expected to be minimal. A typical composition for the infiltrant is 60 at.% Cu, 20 at.% Ni and 20 at.% Mn. Studies using the thermodynamic software, Thermo-Calc, showed that minimal reaction occurs between Mo and the 60Cu-20Ni-20Mn alloy. This can be seen in the phase fraction plot in Figure 2-5. There are two phases at higher temperatures, bcc and liquid. Figure 2-6 shows that the bcc phase is almost pure Mo at temperatures below 1300 °C. It can be clearly seen that there is no solubility for Ni and Mn in the Mo phase at 1200 °C and around 1 at.% Cu is in solution with Mo at 1200 °C. Also Figure 2-7 shows the elemental composition of the liquid phase as a function of temperature. It is evident that the liquid phase consists of primarily Cu, Ni and Mn. However the solubility of Mo in the liquid phase increases with temperature. At around 1200 °C there should be about 1-2 at.% Mo in the liquid. However, the low diffusivity of the refractory Mo would prevent the Mo from dissolving and diffusing through the liquid thus preventing excessive erosion.

Another potential advantage was the low expected shrinkage during sintering due to the refractory nature of Mo. Dimensional control was expected to be a lot better for the Mo/Cu-Ni-Mn system due to the low expected shrinkage, minimal expected reaction

between Mo and Cu-Ni-Mn and the low expected distortion from the age hardening treatment.

It was very hard to predict the porosity control in advance. It would depend on several factors like the solubility of hydrogen in the liquid Cu-Ni-Mn, the solidification shrinkage of Cu-Ni-Mn, and the wetting between the Cu-Ni-Mn and Mo etc.

The biggest advantage of the Mo/Cu-Ni-Mn system was the fact that it is heat treatable. The hardness level of the infiltrant can be tailored according to the specific application. The finish machining could be done in the as infiltrated part which is in the soft state and then the part could be age hardened.

Another advantage of the Mo/Cu-Ni-Mn as compared to the 420/bronze system is the elimination of a softening treatment like annealing.

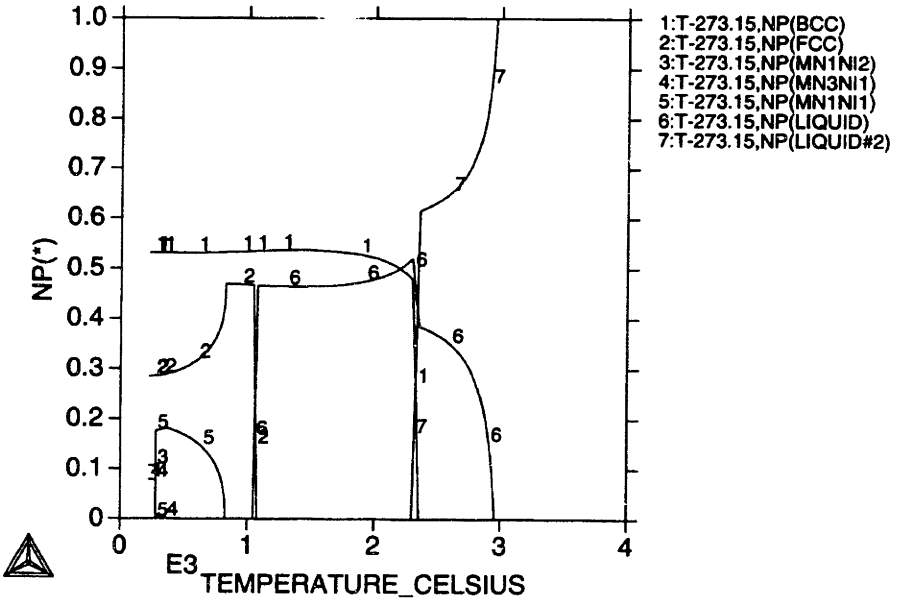

Figure 2-5 : The phase mole fraction versus temperature plot for Mo/60Cu-20Ni-20Mn.

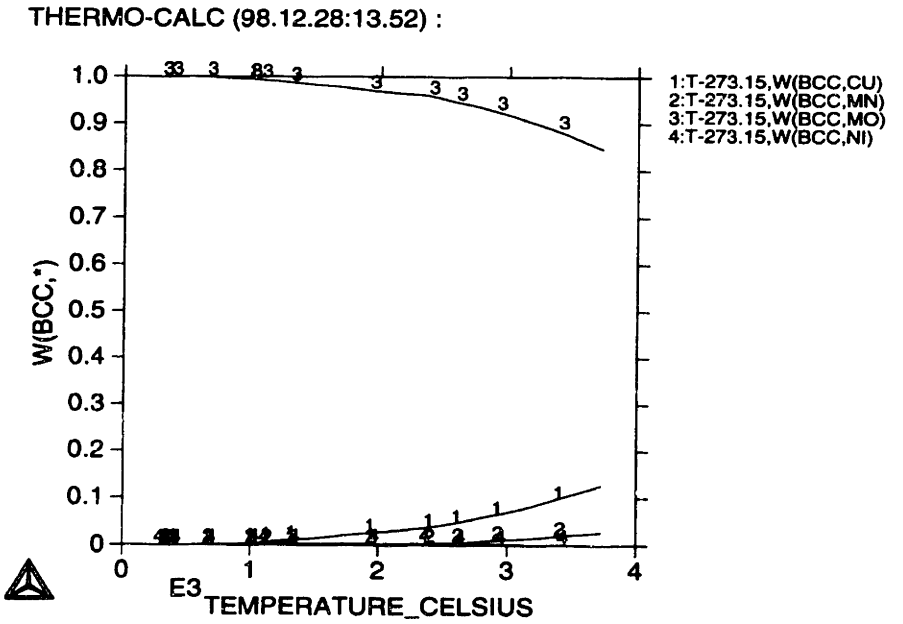

Figure 2-6 : The elemental composition versus temperature for the bcc phase in Mo/60Cu-20Ni-20Mn.

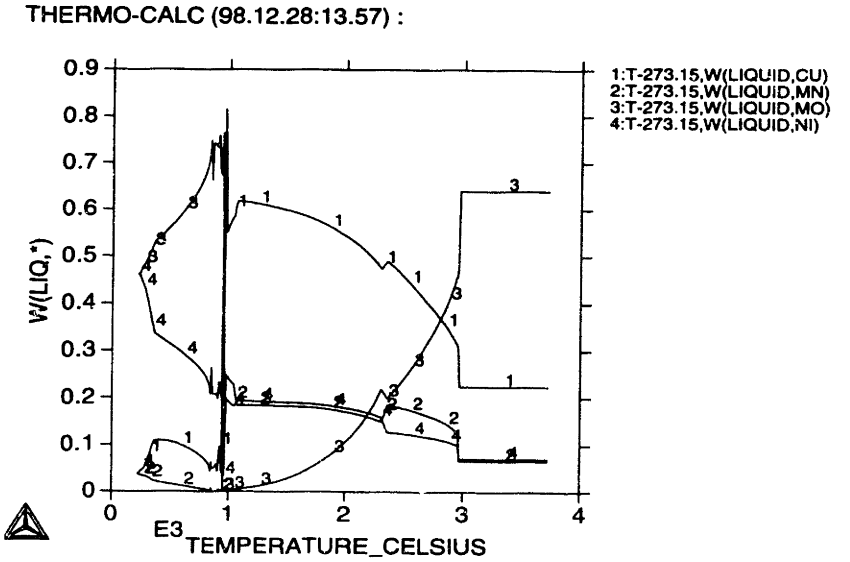

Figure 2-7 : The elemental composition versus temperature plot for the liquid phase in Mo/60Cu-20Ni-20Mn.

2.3.2 Potential concerns with the Mo/Cu-Ni-Mn system

The main concern with this material system was its Electro Discharge Machining (EDM) characteristics. EDM is a commonly used machining technique for injection molding tools. The expected poor behavior of this system was due to the high melting point of Mo which could cause significant electrode wear during the EDM process. A solution to this problem is to use a powder with a lower melting point like 420 stainless steel along with the Cu-Ni-Mn infiltrant. However, previous studies have shown that the two react very strongly [4]. The Cu-Ni-Mn infiltrant is very aggressive and is inert to very few metals, Mo being one of them (others are W and Ta). A possible solution which is discussed later in the thesis is to coat the 420 steel particles with a diffusion barrier like TiC and then infiltrate it with the Cu-Ni-Mn infiltrant.

Other concerns with the Mo/Cu-Ni-Mn were the high price of spherical Mo powder and the high density of Mo compared to tool steel. The high density of Mo would result in the parts being very heavy. Hence, slumping was a potential threat during infiltration. The corrosion resistance of Mo and Cu-Ni-Mn was another concern because Mo has been known to oxidize at higher temperatures.

3 Printing of Binder into Mo Powder

This chapter describes the printing of acrysol into Mo powders, including some of the problems that were encountered during the printing of the parts and methodology used in solving them. Printing was done with two different powder sizes (62 μm and 30 μm). The binder used was acrysol because it has proved to work well with the previous powders (420 and 316L stainless steel).

The most important component of a 3DP™ part is the powder used to create it. Powder chemistry, size and shape determine the type of processing necessary, the surface finish of printed parts, and the printing parameters necessary to achieve high quality printing [12].

3.1 Powder characteristics

3.1.1 Powder size

The size of the powder used for 3DP™ parts affects the surface finish of the parts. A smaller powder size will lead to a better surface finish. In addition, smaller powders decrease the minimum layer thickness that may be used, as it is not possible to create a layer thinner than the maximum powder size. Typically the layer thickness is at least twice the average particle diameter.

The powder size also affects the sintering behavior. Smaller powders have a larger surface area and hence a larger driving force for sintering to occur. As a result, there is a larger shrinkage associated with the sintering of smaller powders. This could potentially be a problem with regard to the dimensional tolerance.

3.1.2 Packing density

The degree and uniformity of powder packing affect the sintering behavior and are a primary concern. The shrinkage and strength of the sintered part depend on the packing density. The maximum packing density that can be obtained for mono-modal spherical powders, without deforming the powder particle, is around 60% [12]. Higher packing densities can be obtained by using bimodal powders [5,13].

3.1.3 Flowability

Although there is some powder re-arrangement that occurs when a binder droplet strikes the powder-bed, the main factor determining the green density of a part is the generation of powder layers. It has been shown that powder-beds created with the standard metal powders used in 3DP™ are very near tap density [12]. It can not be assumed that this will be the case for fine powders. These powders have a very high surface area to volume ratio, increasing the effects of inter-particle friction. This decreases the flowability of the powder.

The flowability of the 62μm powder was very good however there were problems with the flowability of the 30μm powder. The flowability is a function of the powder surface roughness, powder shape, powder surface chemistry and powder hardness [12]. A rough surface or a non-spherical shape will decrease the flowability of the powder. SEM studies were carried out to characterize the powder shape and surface roughness. Figures 3-1 and 3-2 show the SEM micrographs for both the powder sizes. Both the powders have a spherical and a smooth surface. Also, the SEM analysis shows no oxide layer on the surface of the powders. However, the 30 μm powder had a lot more fines dispersed in it while the size distribution of the 62 μm powder was quite sharp.

The poor flowability of the 30μm powder might be associated with the presence of very fine particles [12]. Hence one solution might be to disperse the powder in water, allow the

larger particles to settle and then decant the still-suspended fines. Another approach that has been used in the past is ball milling the powder and coating it with a surfactant [12].

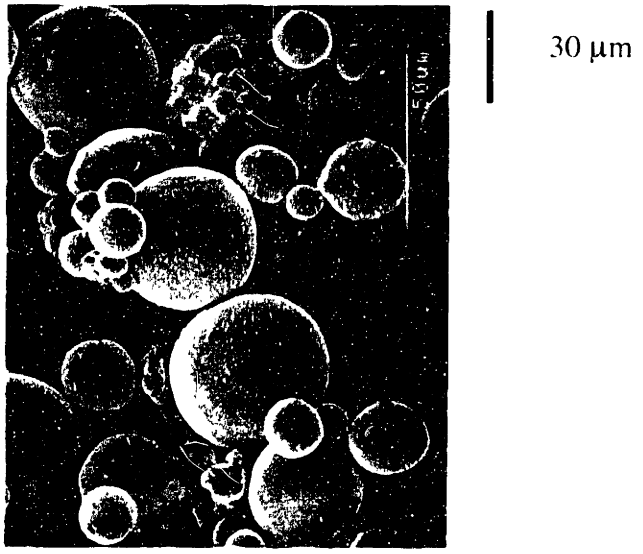

Figure 3-1 : SEM micrograph of the 30 μm Mo powder

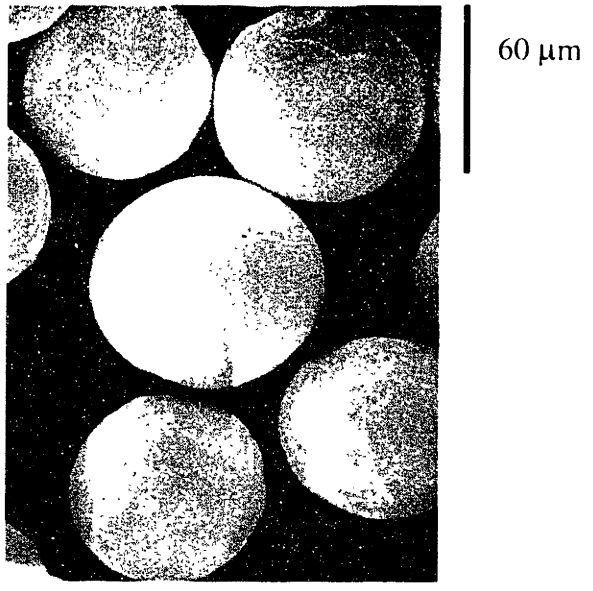

Figure 3-2 : SEM micrograph of the 62 μm Mo powder.

3.2 Problems associated with printing of powders

Similar parts were printed with 62μm and 30μm powders. Figure 3-3 and Figure 3-4 show the parts that were printed. While the part printed with the 62μm powder appeared to have no defects, the part printed with the 30μm powder showed balling. Balling is the break up of a printed line into individual balls of powder and binder. When this occurs, coherent lines are not created and it is not possible to create the desired print geometry. Balling is not observed with the larger powder.

A plausible explanation for balling has been provided [12]. When a droplet of binder strikes the powderbed, it engulfs the particles and penetrates through them. There is a finite amount of time required for this process to be completed, which depends on powder and binder chemistry, binder velocity and powder size. In the formation of a line, droplets are being continually placed next to each other in the powder bed, approximately ½ of a droplet diameter apart. This results in the formation of a cylinder of fluid on the surface of the powder bed. When the length of the cylinder exceeds its diameter, its surface area to volume ratio becomes greater than that of a sphere with the same volume. This creates a driving force that will tend to break the line up into spheres. As the line gets longer, the driving force increases. A slower penetration into the bed will tend to make the line longer. Figure 3-5 shows the reason why the penetration of binder into a powderbed of smaller particles is slower thus resulting in balling. In order to penetrate into the powder bed, the large acrysol droplet has to break up into many smaller droplets. There is an increase in the surface area which translates to an increase in the surface energy. This increase in surface energy opposes the penetration of the droplet. If the particles of powder are finer, the increase in surface area will be more which will result in a larger opposing force. Hence the binder will penetrate more slowly into the bed and accumulation will take place on the surface resulting in balling. This argument ignores the wetting tendency which is the relative value of binder/vapour interfacial free energy (γ) compared with Mo/vapour γ and Mo/binder γ. If the binder wets the Mo then the Mo/binder γ will be less than the Mo/vapour γ and the free energy will go down as the binder spreads and wets more of the Mo.

A more likely reason why balling might be occurring in the 30 μm Mo powder is reduced flow rate of binder into powder due to the higher viscosity in the narrower channels. The narrower channels are associated with higher frictional drag forces which impede the flow of binder.

3.3 Balling and the time interval between droplets

At the beginning of the line, binder penetration is being completed, reducing the length of line that can be considered as fluid. This reduces the driving force for breakup. Balling can be looked at as the outcome of a competition between the deposition of more fluid on the powderbed and its adsorption into the powder bed. If the former dominated, balling will occur and if it is the latter then balling will be avoided.

Figure 3-3 : Part printed with 62 μm Mo powder.

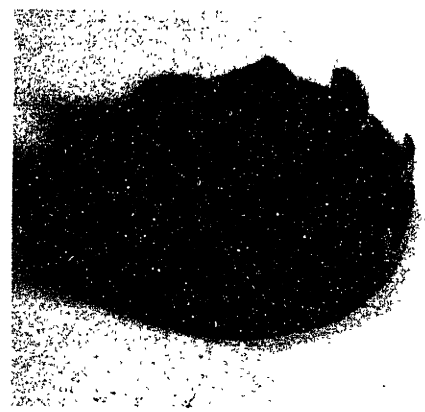

Figure 3-4 : Part printed with 30 μm Mo powder.

There are two ways in which balling can be avoided without changing the characteristics of the powder bed and the binder [12]. The first is to decrease the droplet spacing. This has a twofold effect of increasing the diameter of the printed line and decreasing the rate at which length is added to the line. The downside of this approach is that in certain applications an increase in the line diameter is not desirable. The other approach is to reduce the print frequency while keeping the droplet spacing constant. This will avoid the increase in the line diameter if the droplet spacing were reduced. The disadvantage of this

approach is that a large reduction in print frequency will lead to significantly lower build rates.

In the past fine slurry has been printed into 30 μm Mo powder without any balling occuring. Hence the printing of acrysol into 30 μm Mo powder will have to be worked out in greater detail in order to eliminate balling.

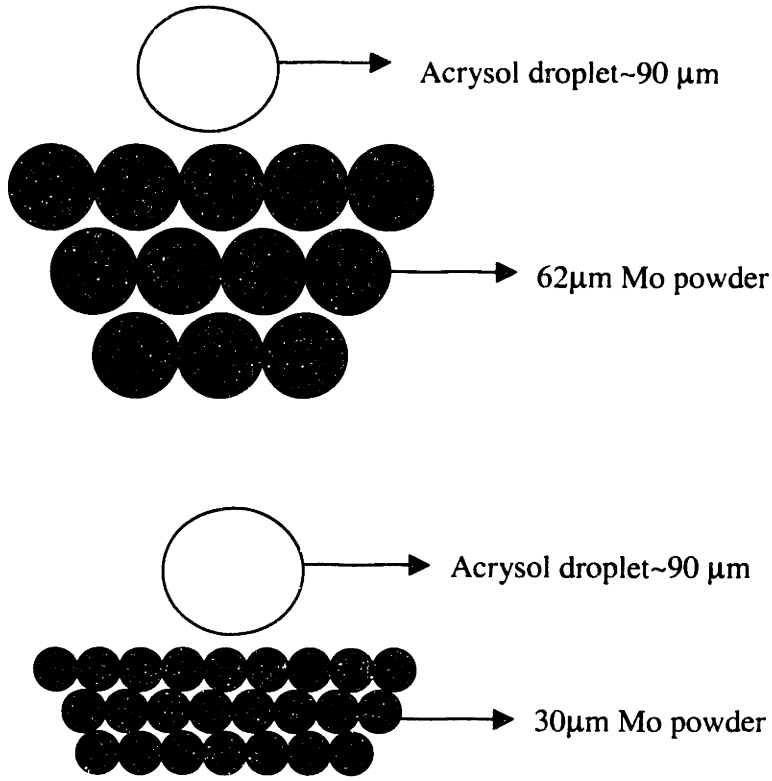

Figure 3-5 : Binder penetration into Mo powder bed.

3.4 Determination of optimal printing parameters

It was decided to focus on producing parts from 62 μm Mo powders because of better results in printing of acrysol into them. Several coupons and parts were printed with 62μm powder. Figure 3-3 shows such a part. The exact printing parameters are listed in Appendix 2. The printing parameters are the same as those that were used while making

the 420/bronze tools. The reason for using the same parameters is the similar size of the powder particles. The parameters result in a binder saturation of 97%.

The acrysol does not form a uniform coating on the powder particle. It exists in a dispersed fashion over the surface of the particle. Figure 3-6 shows the acrysol deposition on the particle. After printing, the parts separated very well from the loose powder with good edge definition.

A tool with conformal cooling channels was printed using the 62 μm Mo powder and acrysol binder. (Figure 3-7) The tool had a very good surface finish and edge definition. It separated very easily from the loose Mo powder. The loose Mo powder was also easily removed from inside the cooling channels.

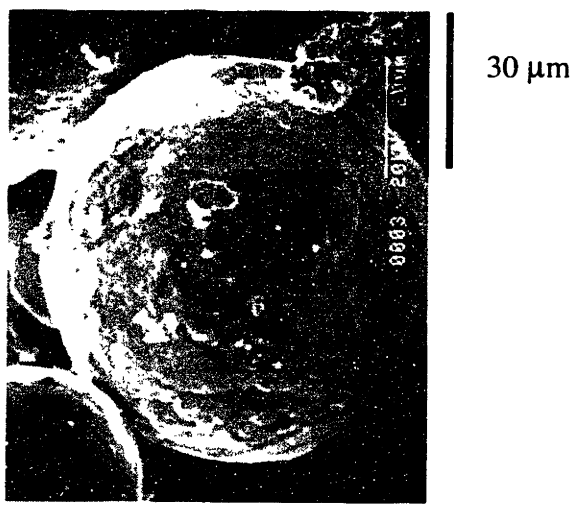

Figure 3-6 : SEM Micrograph of a printed part showing acrysol contact between Mo particles.

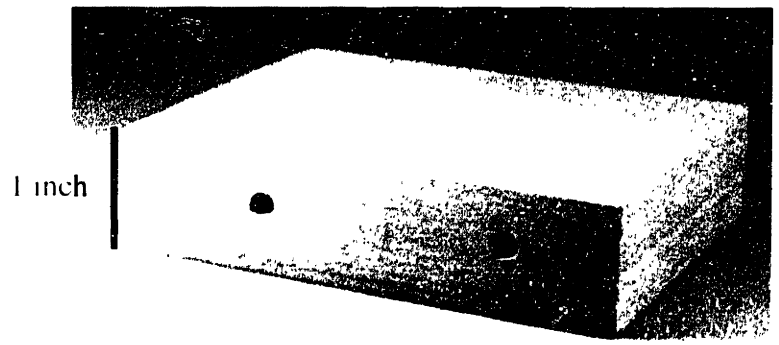

Figure 3-7 : A tool with conformal cooling channels printed using 62 μm Mo powder and acrysol binder.

4 Debinding and Sintering of Mo Powder

4.1 Why debinding and sintering?

The first step in the post processing cycle is the debinding and sintering step. (Figure 1-2) They were separate steps for the previous material system, 420/bronze. However it is possible to combine both the heat treatments into one heat treatment. During debinding. the binder decomposes into volatile and non-volatile products. The volatile products evaporate while the non-volatile products remain as residue. This is necessary before the bonds between adjacent metal particles are formed. This is followed by the sintering treatment where inter-particle bonds ar formed. The amount of sintering is kept small just enough to give the part sufficient strength during the infiltration process. The printed part is buried in zirconia powder during the debinding and sintering process in order to support the skeleton and prevent slumping due to gravity or high-temperature creep.

4.2 Debinding

The debinding treatment for the Mo skeleton is the same as that for the 420/bronze system. This is because the binder material is the same, acrysol. The details of the debinding treatment are given in Appendix 3. The solvent of the binder, water, vaporizes above 100 °C and the organic binder decomposes into volatile and non-volatile components at a temperature around 500 °C. The ramp rate should not exceed 5 °C/min in order to avoid forming blow holes in the part due to the escaping binder gases. However, some binder residues may be left on the surface of the skeleton. It is believed that this residue has a high carbon content and could lead to the formation of a metal carbide phase. The residue of the binder has been found to help bond the skeleton powders together after the debinding and before the sintering, since sintering is very mild until the temperature reaches half the absolute melting temperature of the skeleton (~1200 °C).

4.3 Theory of sintering

Sintering is a solid-state diffusion bonding process among particles. When the temperature is high enough, mass transport occurs from other parts to the neck between particles. This process results in a decrease in surface area and hence in surface free energy. There are several transport mechanisms that can occur during sintering. They have been summarized by Kingrey[14], as: (1) surface diffusion, (2) lattice diffusion from the surface, (3) vapor transport, (4) boundary diffusion, (5) lattice diffusion from the volume and (6) lattice diffusion from grain boundaries. Figure 4-1 shows the various mechanisms that exist during sintering. Mechanisms (1) and (3) are surface transport mechanisms and mechanisms (2), (3), (4), (5) and (6) are bulk transport mechanisms. All transport mechanisms contribute to inter-particle bonding by transporting material from other parts of the particle to the points of contact with other particles where a neck gradually forms.

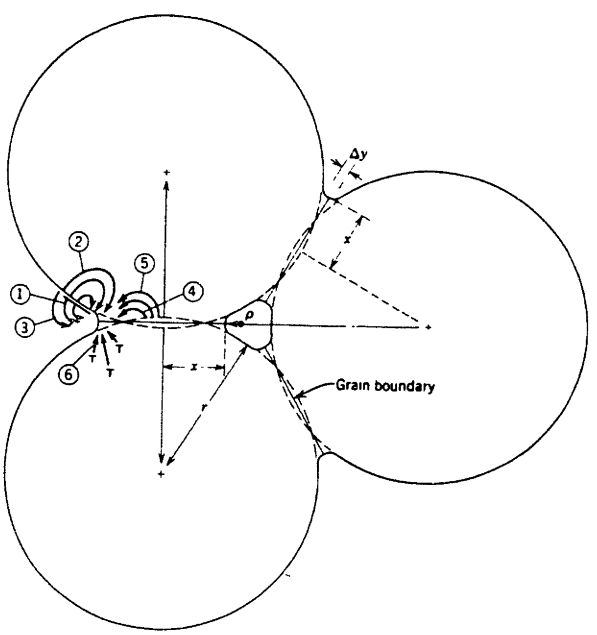

Figure 4-1 : Different transport mechanisms during sintering [15].

4.3.1 Different Transport mechanisms during sintering

4.3.1.1 Surface transport mechanisms

Surface transport mechanisms produce neck growth without a change in particle spacing (no shrinkage or densification) due to mass flow originating at the particle surface and terminating at the neck between the particles. Surface diffusion and vapor transport are the two most important contributors during surface transport controlled sintering. Surface diffusion dominates the low-temperature sintering of many metals, including iron. Vapor transport is not as widespread, but dominates the sintering of low stability materials such as lead and lead-based compounds. Vapor transport has also been observed in certain refractory metals like W and Mo.

4.3.1.2 Bulk transport mechanisms

While both surface diffusion and bulk transport processes promote neck growth, the main difference is that bulk transport mechanisms produce shrinkage while surface activated mechanisms do not. For densification to occur, the mass must originate from the particle interior with deposition at the neck perimeter. Bulk transport mechanisms include volume diffusion and grain boundary diffusion. Grain boundary diffusion is fairly important to the densification of many common systems. Generally bulk transport processes are more active at higher temperatures.

4.3.2 Prediction of Mo sintering shrinkage

Efforts have been made to model the sintering of Mo powder [15]. Appendix 4 gives a more detailed description of the theory behind modeling effort. Figure 4-2 depicts a two sphere model for sintering, where two particles of diameter D are bonding with a neck of diameter X. The neck size ratio is defined as X/D.

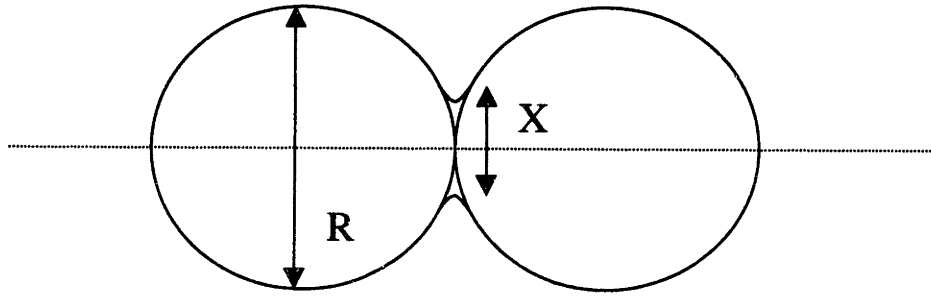

Figure 4-2 : Two sphere model for sintering. [15]

The mass transport processes that have been modeled are surface diffusion, volume diffusion and grain boundary diffusion. Values of diffusivities and activation energies for all the transport processes in Mo are included in Appendix 4 and 6 [15]. An effort was made to model the sintering of Mo using these data. Figure 4-3 shows the predicted contribution of the various transport processes to neck formation as a function of the sintering temperature. It is evident that between 1000 °C and 1500 °C the dominant process is predicted to be grain boundary diffusion with volume diffusion taking the secondary role. Surface diffusion is predicted to be negligible in the desired temperature range. The sintering time for the plot is 12 hours. Figure 4-4 shows the total neck formation (contribution from all the processes) as a function of temperature for two particle sizes (30μm and 62 μm). Larger neck-size ratios are formed between the smaller particles (30 μm). The size of necks formed is on the whole very small and is sensitive to the sintering temperature.

Since surface diffusion does not play a dominant role, the shrinkage obtained should correlate very well with the neck-size ratio. Figure 4-5 shows the predicted shrinkage obtained in the sintering of Mo powder as a function of the sintering temperature. Two phenomena are very evident: (1) The shrinkage obtained is predicted to be increasingly sensitive to the sintering temperature and (2) the shrinkage is predicted to be greater in the smaller particles. Figure 4-6 shows the predicted sensitivity of time in the sintering process. The shrinkage becomes decreasingly sensitive to time after a certain critical

number of hours. In conclusion, sintering theory shows that the necks formed and the shrinkage obtained are very sensitive to particle size and sintering temperature. The sintering time does not play an important role after it exceeds a certain critical amount.

4.3.3 Acrysol residue after debinding

Acrysol is the polymeric binder that glues the Mo particles together during the printing process. Although it is supposed to evaporate during the debinding step at 500 °C, experiments have indicated that some carbon residue might be left over between the particles. Experimental work has shown no direct evidence of this residue. In a study conducted [16], phase diagrams have been used to explain the formation of Mo_2C, Mo or MoO_2 as a function of the sintering atmosphere and temperature. Figure 4-7 shows two phase diagrams at 1200 K and 1800 K where the stability of the various phases is plotted as a function of the partial pressures of carbon monoxide (P_{CO}) and oxygen (P_{O2}) content. It can be seen that as the temperature decreases, the P_{CO} required to form Mo_2C tends to decrease and the triple point shifts. The dew point in the furnace has been measured to be -20 °C or lower at the debinding temperatures. The P_{CO} values were not measured but are expected to be on the high side at the debinding temperatures due to the presence of more carbon in the system. Both these factors could stabilize the Mo_2C phase at the debinding temperature, 200-500 °C (473 K-773 K). At higher temperatures like the sintering temperature (1200 °C), the P_{CO} is expected to drop due to depletion of carbon from the system. This could stabilize the Mo phase and release the carbon. This could be a possible explanation for the acrysol residue after debinding and its effect on sintering at 1200 °C.

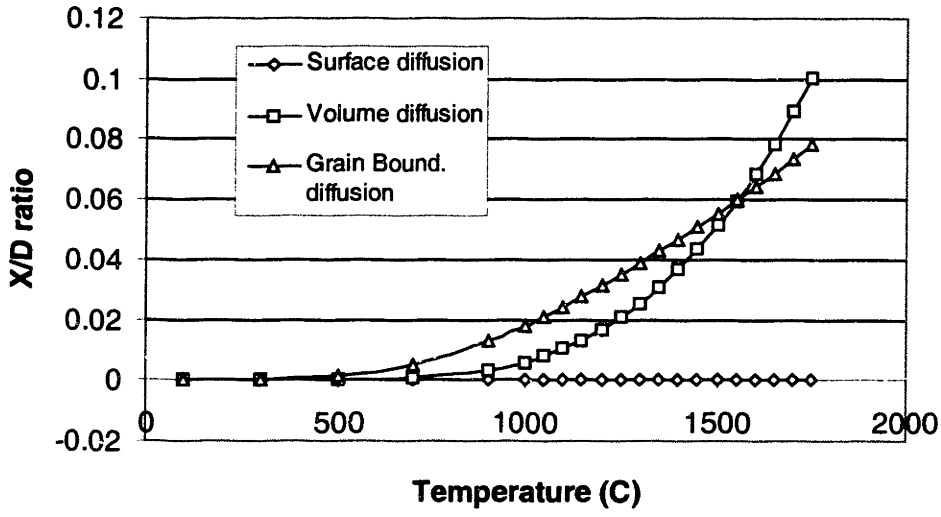

Figure 4-3 : Contribution of the various transport processes to the neck size in the sintering of 62 μm Mo powder for 12 hours.

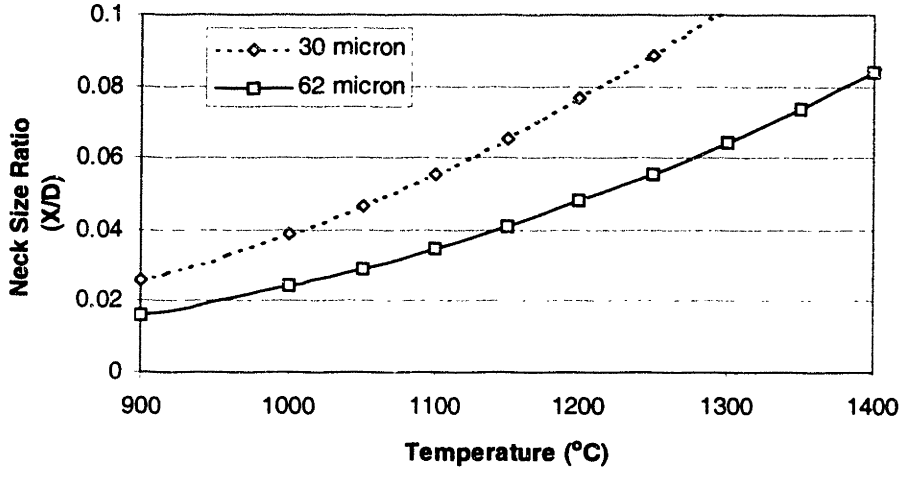

Figure 4-4 : Total neck size versus sintering temperature for 30 μm and 60 μm Mo powders sintered for 12 hours.

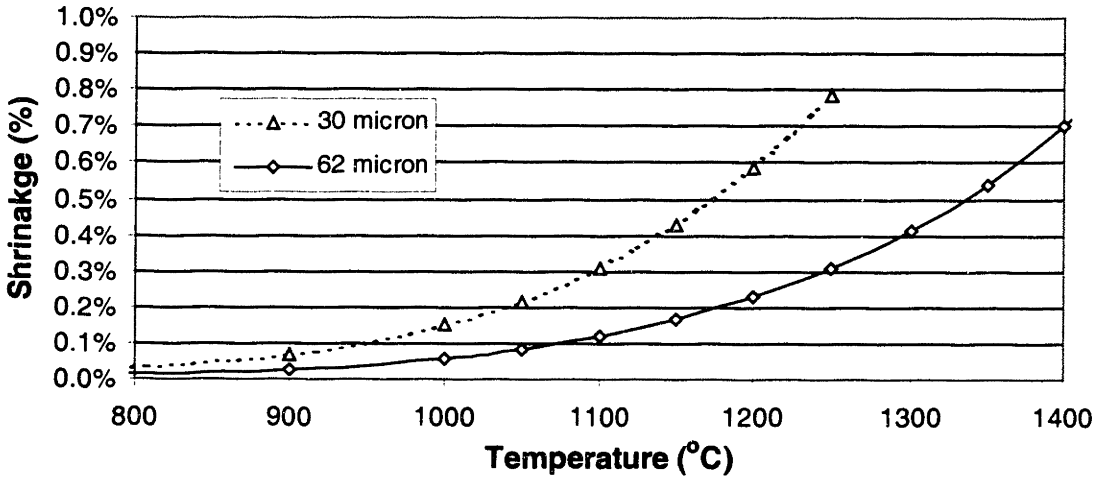

Figure 4-5 : Shrinkage versus sintering temperature for 30 μm and 62 μm Mo powder sintered for 12 hours.

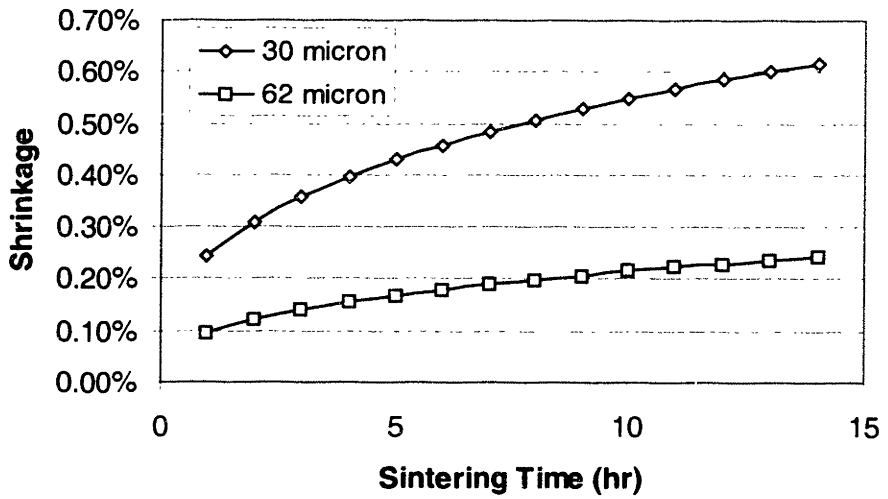

Figure 4-6 : Shrinkage versus sintering time for the 30 μm and 62 μm Mo powders sintered at 1200 °C.

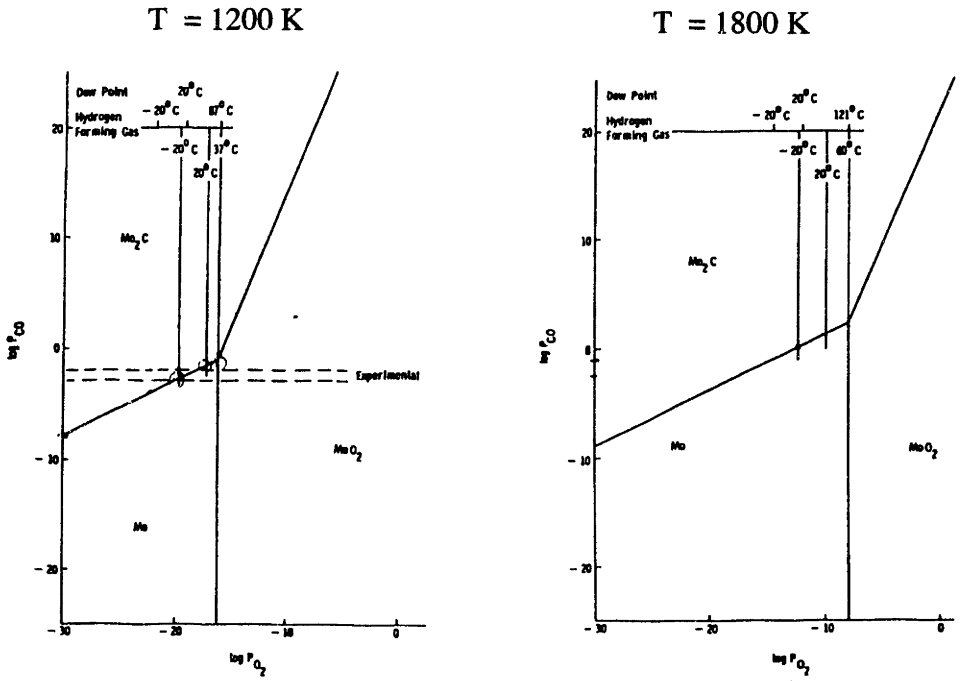

Figure 4-7 : Mo/O/C phase diagrams at 1200 K and 1800 K. [Young]

4.4 Various experimental test procedures to study the sintering of Mo

Several of the experiments that were carried out to study the sintering of Mo have been conducted previously [17]. The strength of the sintered part was very critical and it depended on the size of the necks between particles. Earlier studies (Figure 4-4) showed that the neck size was very sensitive to the sintering temperature and particle size. Hence the goal was to determine the optimal sintering temperature and particle size. The various tests can be divided into two categories, determination of sintering temperature and determination of shrinkage. All the sintering experiments were carried out in a forming gas atmosphere in order to prevent oxidation.

4.4.1 Determination of critical sintering temperature (Ts)

The critical sintering temperature (*Ts*) is defined as the minimum temperature where a part sintered for 4 hours will have sufficient strength. To determine this temperature a

simple series of tests were conducted. 15ml of powder was placed in a crucible that was fired to different temperatures and held for 4 hours. The ramp-up and cool-down rates were 10 °C/min. The temperature was varied from 900 °C to 1300 °C. The firing was done in an alumina tube furnace shown in Figure 4-8, in a forming gas (95% argon + 5% hydrogen) atmosphere. The gas flow rate was held to 5 SCFH. After firing, the samples were placed in an ultrasonic bath (Sonicor TS-3047HC), as shown in Figure 4-9. Samples that broke down in a few seconds did not have sufficient strength. This was a consequence of the fact that they had not formed necks of sufficient size. These tests were carried out for the 30 and 62 μm Mo powders.

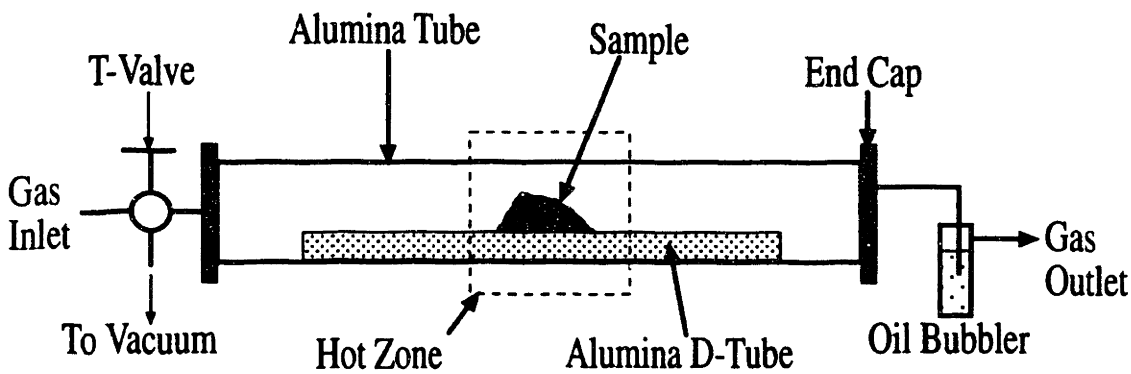

Figure 4-8 : Schematic of the alumina tube furnace [17].

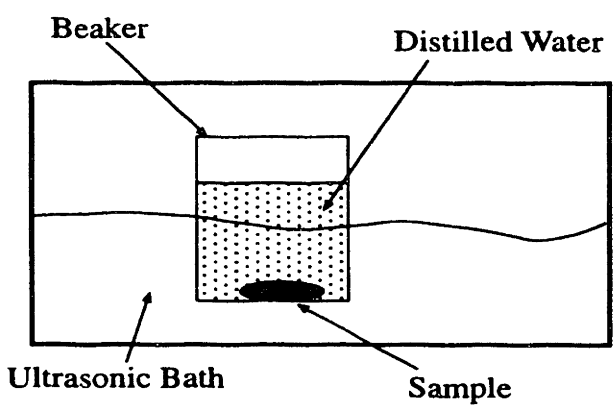

Figure 4-9 : Schematic of the ultrasonic bath [17]

4.4.2 Shrinkage tests

Several tests were carried out to measure the shrinkage in Mo. The two main tests are described below.

4.4.2.1 Fiducial mark technique

Small coupons (1/2"x 1/4"x 1/4") with fiducial marks were printed using 62μm and 30μm powders and acrysol. (Figure 4-10) The coupons were placed on an X-Y stage. The distance between the fiducial marks was measured using an optical microscope. Under high magnification, it was observed that the fiducial lines were not straight and the powder particles along the line were not aligned. The edge position had an amplitude of about four powder particles (Figure 4-11). Hence there was an error of a few particle sizes in the distances measured. Calculations showed that the actual change in length for the coupons was on the order of two particle sizes (~120 μm). Hence this method was not capable of measuring shrinkage accurately.

4.4.2.2 Pin technique for shrinkage measurement.

A more accurate technique for measuring the shrinkage in Mo powders based on the work by Yoo [17], was used. A rectangular alumina tray was filled with powder. Small pins made from a SiC fiber were placed in the powder as shown in Figure 4-12. The diameter of the SiC pins was 30 μm and there was an inner carbon core of diameter 5μm within the fiber which was very distinctly visible. This was used as a reference point. A pipette was used manually to saturate the regions between each pair of pins with the acrysol binder.

Figure 4-10 : Printed coupons with fiducial marks, 62 μm Mo powder.

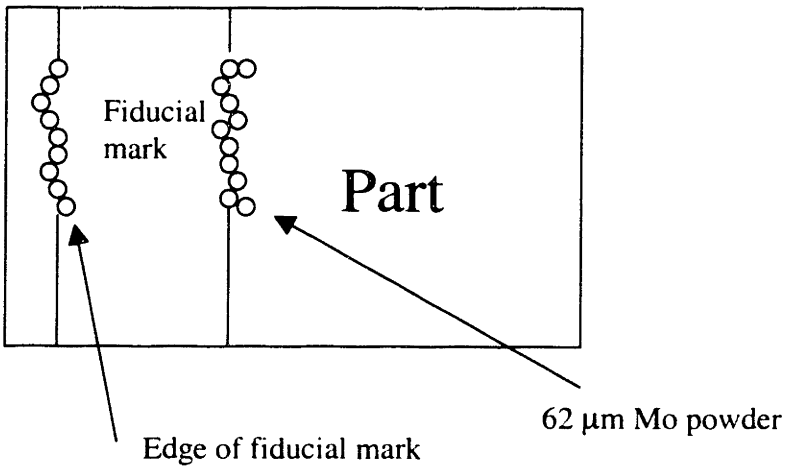

Figure 4-11 : The zigzag edge of the fitucia mark on the part, 62 μm Mo powder.

Care was taken that the saturated regions did not join together or extend to the walls of the crucible. (Figure 4-12). An optical microscope with a micrometer driven X-Y stage was used to measure the distance between the pins. The surface was covered with an additional layer of loose powder to protect if from any oxidation. After the sintering heat treatment, the crucible was removed from the surface and the distances were re-measured. The error in the measurements was at most ~5μm (diameter of the inner carbon core).

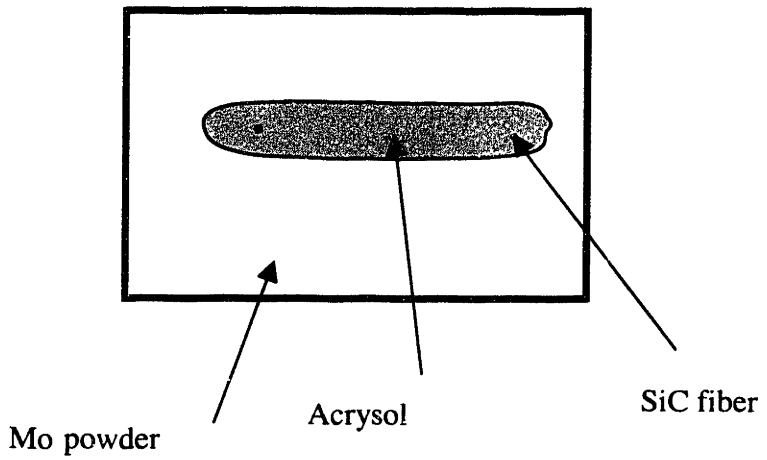

Figure 4-12 : Shrinkage pins in a bed of 62 μm Mo powder.

4.5 Observed sintering behavior

Table 4-1 shows the results obtained from the sintering temperature tests. Coupons printed with 30μm and 62μm powder were subject to different sintering temperatures for 1 hour. If they subsequently dispersed fully or partially in the ultrasonic bath, it meant that the strength was inadequate and the necks formed were too small. These studies demonstrated several important findings. (1) There is a critical sintering temperature above which the strength of the coupon is adequate and the necks formed are large enough. (2) The acrysol residue aids in the sintering process and enables the formation of larger necks thus lowering the critical sintering temperature. (3) The sintering is significantly faster in the smaller particles leading to higher neck particle size ratios. This results in a lower critical sintering temperature for the smaller particles. For the 62μm coupon printed with acrysol, the critical temperature, where adequate strength is obtained, is 1200 °C. On the other hand, the critical sintering temperature for the 30 μm Mo with acrysol was 1100 °C. When acrysol was not used, the *Ts* was above 1200 °C for both the 62 μm and the 30 μm Mo powders.

Sintering Temperature	Pure Mo(30 μm)	Mo(30 μm) + acrysol	Pure Mo(62 μm)	Mo(62 μm) + acrysol
900 ° C	D	PD	D	D
1000 ° C	D	PD	D	PD
1100 ° C	PD	ND	D	PD
1200 ° C	PD	ND	PD	ND
D=Dispersed in sonicator	PD= Partially dispersed in sonicator		ND=No dipersion in sonicator	

Table 4-1 : Results from the sintering temperature experiments for 30 μm and 62 μm Mo powders sintered for 4 hours.

Once the critical sintering temperature was obtained, in order to develop the sintering treatment a study was conducted to predict the effect of sintering time on neck formation and shrinkage (Table 4-2). The experiments were carried out on 30μm and 62μm coupons with and without acrysol. Again, the effect of acrysol is very evident. The sintering temperature for all the experiments was 1200 °C (critical sintering temperature for 62 μm Mo with acrysol). The shrinkage obtained for the pure Mo powders at 4 hours and 12 hours correlates very well with that predicted by theoretical modeling in Section 4.3.2 (Figures 4-6). The coupons that were printed with acrysol show a slightly higher shrinkage. On the other hand, the sintering strength increases with the use of acrysol. This means that the acrysol residue is behaving like a sintering activator. It is also evident that the shrinkage increases with time and that the 30 μm particles sinter more and undergo greater shrinkage.

Sintering Time	Pure Mo(30 μm)	Mo(30 μm) + acrysol	Pure Mo(62 μm)	Mo(62 μm) + acrysol
4 hours	0.42%	0.48%	0.14%	0.23%
12 hours	0.57%	0.71%	0.20%	0.32%

Table 4-2 : Results from the shrinkage tests for 30 μm and 62 μm Mo powder sintered at 1200 °C.

Figures 4-13 and 4-14 illustrate the effect of sintering time in 62 7μm Mo with acrysol. It can be seen that the powder that was sintered for 12 hours shows a larger neck size ratio as compared to the powder that was sintered for 4 hours. Also notice that the surface

grain boundary grooves are etched more in the powder that was sintered for 12 hours. Hence, the neck grows and the surface grain boundaries get more etched with time. This is a clear indication of the presence of surface transport during sintering. As a result of the increase in neck size ratios, the strength also increases with time.

4.6 Effect of acrysol in sintering

As observed in the previous section, the acrysol does behave like a sintering activator, enhancing mass transport processes. It is evident from the experiments that acrysol accelerates the neck formation process while not leading to significantly more shrinkage. Hence, it must be activating the surface diffusion in the Mo. A higher surface diffusion would lead to larger necks and higher strength but not more shrinkage. Figure 4-15 and 4-16 show the effect of acrysol in 30μm Mo. The powders containing acrysol show more neck formation and etching on the surface of the particle, again consistent with an acrysol product activating surface transport. Note the broken necks on the surface of the powder that was sintered along with acrysol residue. Young has studied the sintering of 50 μm Mo powder with a polymeric binder. He also concluded that polymeric binder residues tend to activate the surface diffusion during the sintering of Mo powder [16].

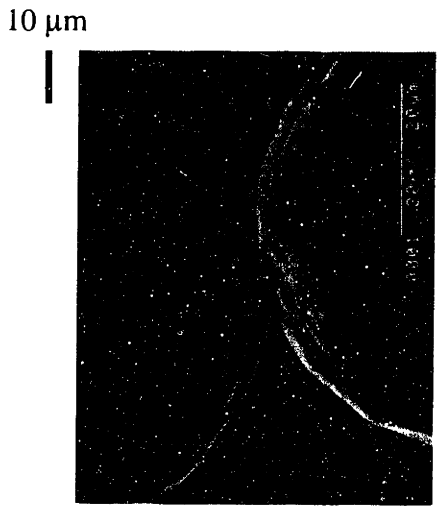

Figure 4-13 : Micrograph of 62 μm Mo powder with acrysol, sintered at 1200 °C for 4 hours.

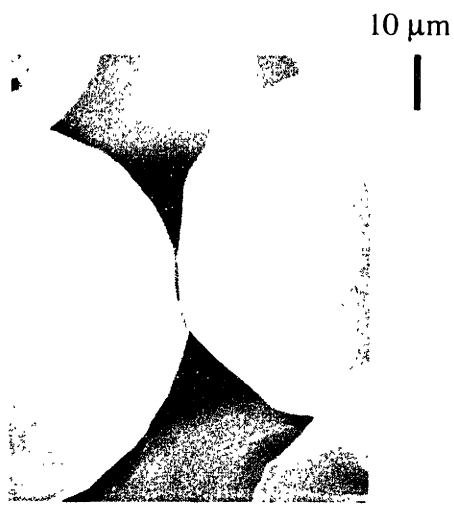

Figure 4-14 : Micrograph of 62 μm Mo powder with acrysol, sintered at 1200 °C for 12 hours

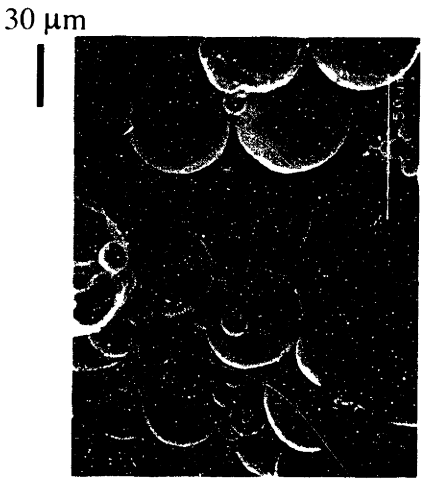

Figure 4-15 : Micrograph of 30 μm Mo powder without acrysol, sintered at 1200 °C for 12 hours.

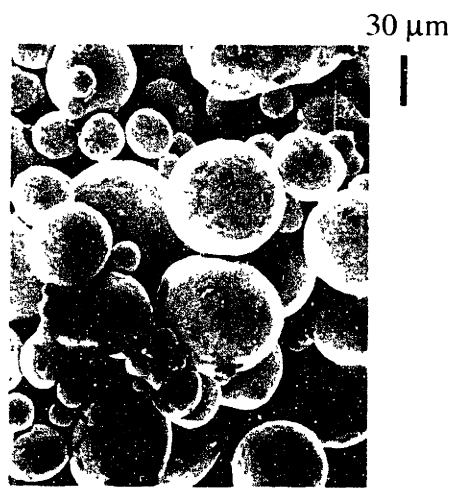

Figure 4-16 : Micrograph of 30 μm Mo powder with acrysol, sintered at 1200 °C for 12 hours.

4.7 Optimal debinding and sintering treatment

After studying the results from the experiments a detailed sintering treatment was developed for the 62 μm powder. This treatment is given in detail in Appendix 3. It essentially involves holding the part first at 200 °C for ½ an hour, then at 500 °C for another ½ an hour and then at 1200 °C for 12 hours. The sintering temperature was selected as 1200 °C for two reasons: (1) The critical sintering temperature was experimentally found to be 1200 °C for the sintering of 62 μm Mo powders, with acrysol binder. (2) It is the maximum service temperature the furnace available could handle without leading to other problems. A sintering time of 12 hours was used in order to improve the strength. Although the strength of the part was sufficient to withstand infiltration, it was still not adequate. The part was very fragile and required very careful handling. In order to obtain a better strength, a higher sintering temperature or a smaller particle size would be more appropriate.

Appendix 6 contains data on diffusion in Mo. From the data on diffusion in Mo it is apparent that the surface diffusion in Mo dominates at 1200 °C.

The shrinkage in the coupons that are subject to this treatment is 0.32%. The sintering experiments were run in a forming gas atmosphere in the tube furnace and the MRF furnace. There was no difference in the results between the tests carried in the two furnaces.

The sintering shrinkage observed in the two tools that were manufactured for Motorola is given in Appendix 9. Figure 4-17 shows such a tool with conformal cooling channels which was sintered at the optimal treatment. The measurements were taken using vernier calipers. It can be seen that the shrinkage obtained is an-isotropic and slightly lesser than that obtained on the test coupons. Also, the shrinkage along the smallest dimension perpendicular to the printed layers was always the least.

Figure 4-17 : 62 μm Mo tool sintered at 1200 °C for 12 hours.

5 Infiltration

5.1 Why is infiltration required?

One way of fully densifying the part is to sinter it to full density. Mo has a fairly high melting point (~2610 °C). Therefore at 1200 °C there is very little transport due to the low diffusivities. This makes sintering to full density impossible for large size Mo particles (~62 μm). In order to sinter to full density, a very high temperature will be required which cannot be attained in any furnace currently available at MIT. Even if sintering to full density were possible it would still be undesirable because full densification would lead to high shrinkage. This would very likely deteriorate the dimensional accuracy of the part. An alternative process to fully densify the part is to infiltrate the lightly sintered powder "skeleton" with a low melting alloy at an elevated temperature where the alloy melts and flows into the porous skeleton. The low melting alloy is commonly known as the "infiltrant". In the course of the infiltration process, the liquid infiltrant flows into the continuous porous skeleton by capillary action and fills the voids. The process is similar to a sponge absorbing water. Once the skeleton has been infiltrated, a near net-shape tool is ready for finish machining.

The main reason for infiltration is to enhance the mechanical properties of the part. Achieving a fully dense structure allows a part to contain the necessary pressure inside the cooling channels. In addition, thermal and electrical conductivity improve along with the toughness of the part. The machinability of an infiltrated part is a lot better than the porous skeleton because it facilitates continuous chip formation. A skeleton probably machines by having the particles rip off.

5.2 Cu-Ni-Mn as an infiltrant. Important Issues:

The Cu-Ni-Mn infiltrant is age hardenable, with optimum age hardening response at approximately 60at.% Cu, 20at.% Ni and 20at.% Mn. Hence forth Cu-Ni-Mn will refer to the alloy of optimal composition. The melting point of the infiltrant is around 1040 °C. The infiltration temperature must be at least 50 °C above the melting point of the infiltrant in order to provide adequate viscosity in the infiltrant. This is important for the capillary action required in the infiltration process. There are several important criteria that the infiltrant should satisfy.

5.2.1 Reaction between Mo and infiltrant (Thermocalc work)

The binary systems Mo-Ni, and Mo-Mn were studied to predict the solubility of both Ni and Mn in Mo. The phase diagrams have been included in Figures 5-1 and 5-2 [18]. From the phase diagrams it is evident that Ni and Mn have considerable solubility in Mo. On the other hand, Mo has very little solubility in Ni and considerable solubility in Mn. Hansen has studied the Mo-Cu phase diagram and claims that a liquid-liquid miscibility gap exists [21]. The solubilities in the solid are vanishingly small.

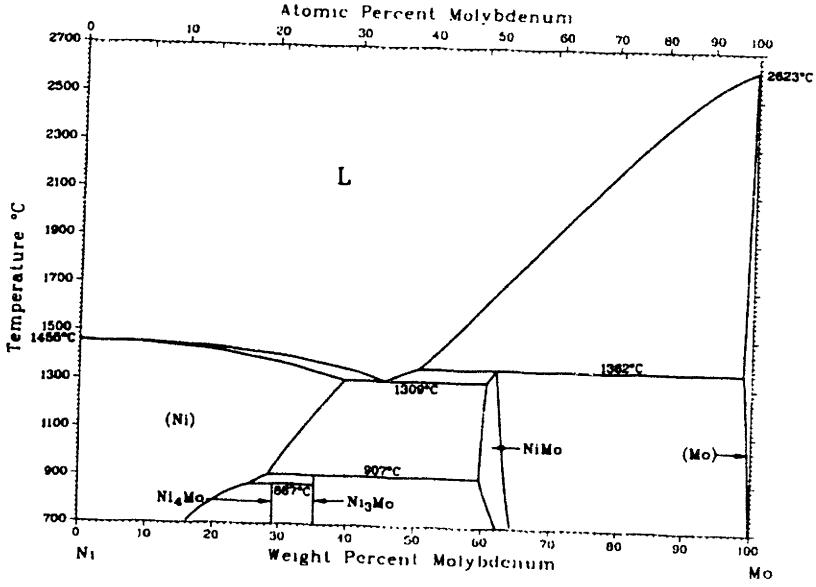

Figure 5-1 : The Mo-Ni phase diagram.

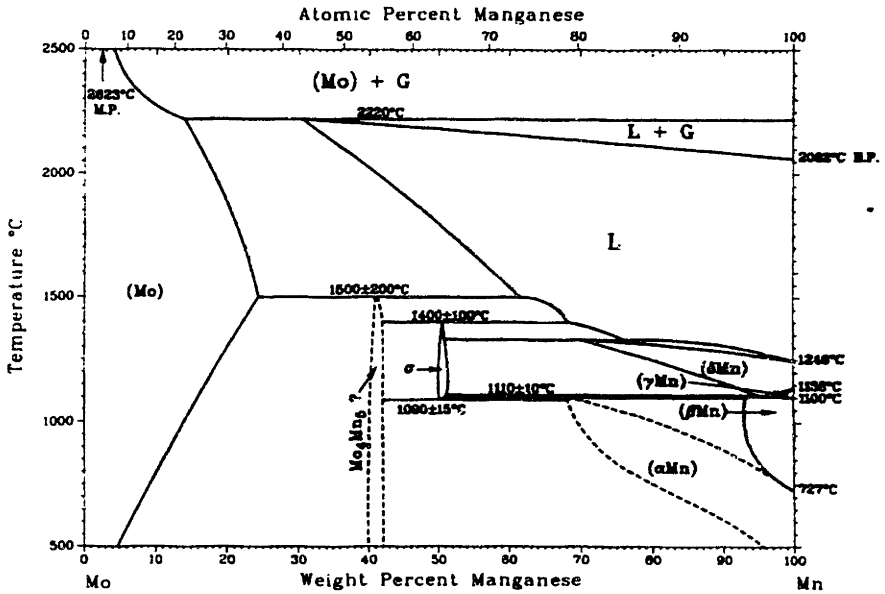

Figure 5-2 : The Mo-Mn phase diagram.

The Mo-Cu-Ni-Mn quaternary system was modeled using Thermo-Calc software and was studied to predict the reaction between the Mo skeleton and the 60Cu-20Ni-20Mn infiltrant. The "KP" database was used for this system. Data on the L_0 and L_1 parameters for the Cu-Mo system were missing. These parameters were estimated by trial and error. The phase fraction plot for the quaternary system has been is illustrated in Figure 5-3. At 1200 °C the equilibrium phases are the bcc phase and the liquid. Figures 5-4 and 5-5 show the elemental composition of these phases. At 1200 °C, the bcc phase is primarily Mo and the liquid phase is rich in Cu, Ni and Mn. This proves that at thermodynamic equilibrium there is very little Cu, Ni or Mn in Mo and vice-versa. Hence, very little reaction is expected between the solid Mo skeleton and the liquid Cu-Ni-Mn infiltrant at 1200 °C. However, it should be noted that the solubility of Mo increases as the temperature exceeds 1200 °C.

The refractory nature of Mo will result in very low diffusivities which will reduce the tendency for any inter-diffusion between the Mo skeleton and the infiltrant.

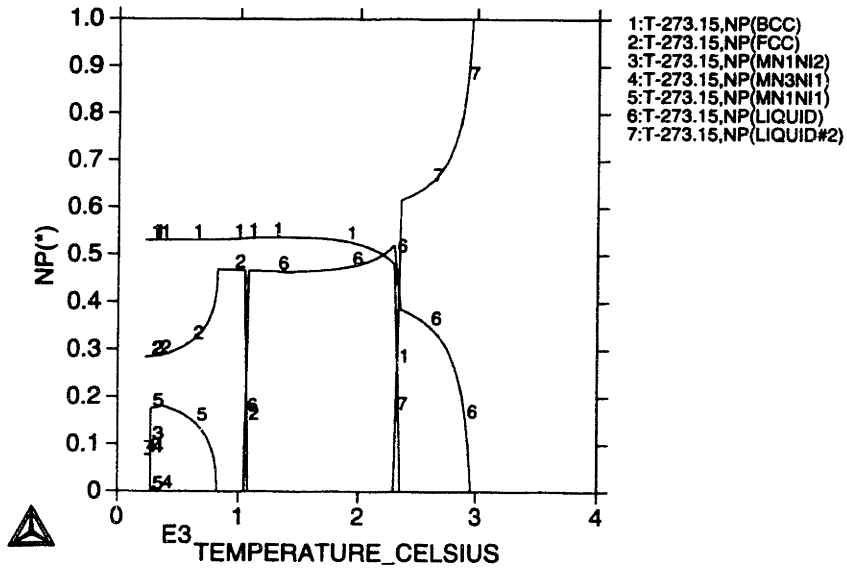

Figure 5-3 : The phase mole fraction versus temperature for Mo/60Cu-20Ni-20Mn.

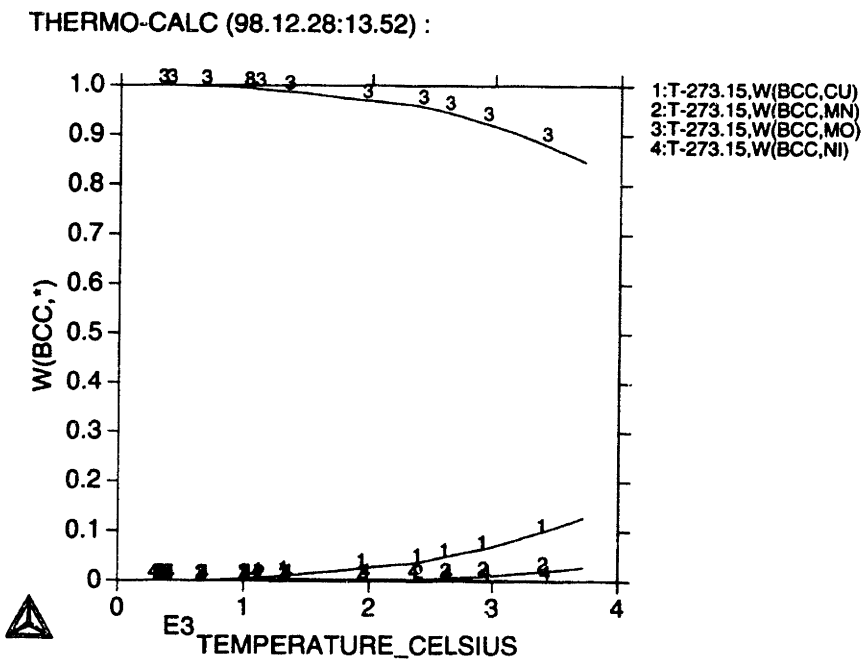

Figure 5-4 : The elemental composition versus temperature plot for the bcc phase in Mo/60Cu-20Ni-20Mn.

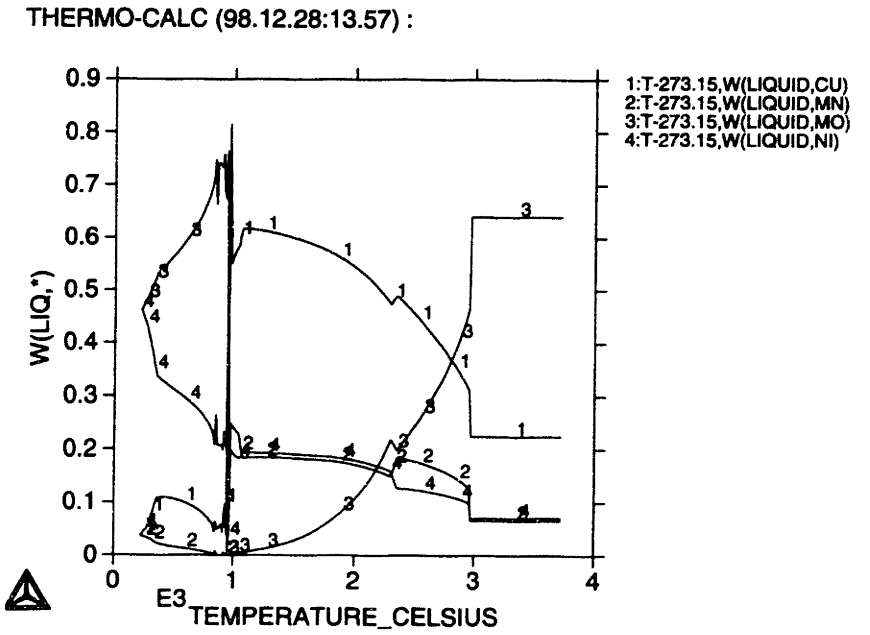

Figure 5-5 : The elemental composition versus temperature plot for the liquid phase in Mo/60Cu-20Ni-20Mn.

Even if the reaction between the skeleton and the infiltrant were thermodynamically feasible, it would be kinetically unfeasible due to the large difference in the melting points between the infiltrant and the skeleton. The diffusivity of the Cu, Ni and Mn atoms in solid Mo would be very small.

5.2.2 Wetting and capillary issues

Studies on the wetting of Mo by Cu alloys have been carried out by previous researchers [19]. The degree of wetting is measured by the wetting angle θ between the liquid infiltrant and the substrate. Figure 5-6 is an illustration of the wetting angle 'θ'. The cosine of the wetting angle is proportional to the capillary force for infiltration. Hence, the smaller the θ, the better the wetting and the greater the force. Figures 5-7 and 5-8 illustrate the effect of time, temperature and atmosphere on the wetting of Mo by copper alloys [19]. Figure 5-7 depicts the wetting angle for several copper alloys with Mo as a function of time. It is evident that a steady-state value is achieved at short times. Figure 5-8 gives the wetting

angle of a copper alloy under forming gas and inert atmospheres [19]. The wetting was markedly improved for the forming gas atmosphere because of its reducing nature. Any oxides formed on the substrate surface will be immediately reduced, thus improving the wetting. On the other hand the oxides impede the wetting in an inert gas atmosphere. It is also evident that the wetting improves as the temperature increases.

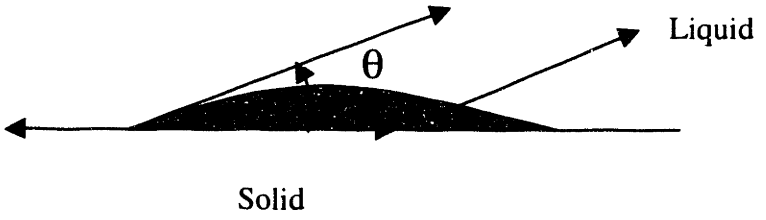

Figure 5-6 : Illustration of wetting angle 'θ' [19].

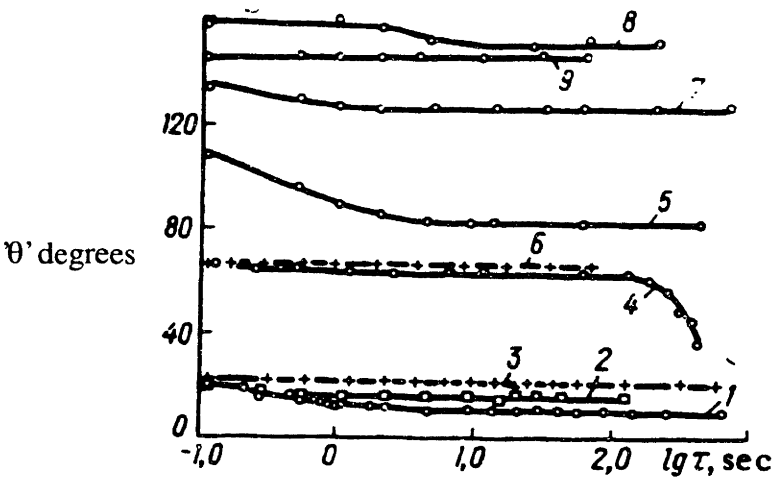

Figure 5-7 : Effect of time on wetting angle 'θ' [19].

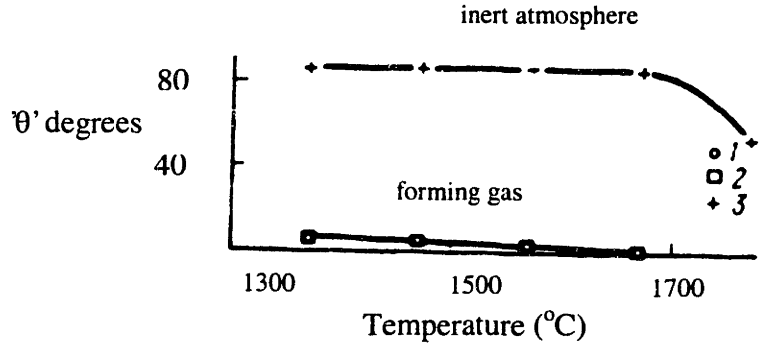

Figure 5-8 : Effect of atmosphere on wetting angle 'θ'.

The maximum height to which the infiltrant can rise has been calculated for the Mo/Cu-Ni-Mn system assuming perfect wetting, θ=0 degrees. The rough calculations are included in Appendix 5. The maximum height was calculated as roughly 1 meter for 62 μm Mo powder. Since the hydrogen atmosphere is even more reducing than the forming gas atmosphere, it is expected to enable better wetting.

5.2.3 Porosity control

The solidification range of the Cu-Ni-Mn infiltrant is relatively narrow (1040-1060°C) [20] compared to Cu-10Sn (bronze). This would reduce the size of the dendrite arms during solidification and make it easier for the liquid infiltrant to flow into the root of the dendrite cavity. Hence, there will be reduced tendency to form connected porosity due to gas trapped along the dendrite arms during solidification [9].

There is no data on the solubility of hydrogen gas in the liquid and solid 60Cu-20Ni-20Mn. If the data for pure copper or bronze can be extrapolated, there will be a large solubility difference of hydrogen in the liquid and solid infiltrant. The solubility of hydrogen in liquid and solid copper at the melting temperature is 5 cm^3 and 0.5 cm^3 of H_2 gas per 100 grams of copper, respectively [21]. As the liquid solidifies, the solubility decreases sharply. The excess gas may not have sufficient time to escape. Hence this could lead to porosity during infiltration. However if this were the case then the heat treatment could be modified to counter this phenomena. The ramp up could be carried out

initially in hydrogen until the temperature reaches the solidus temperature. The atmosphere could then be changed to vacuum or inert gas. This would prevent dissolving of any gas in the liquid infiltrant and also purge the liquid infiltrant of any existing gas bubbles.

Another reason for porosity could be the solidification shrinkage in 60Cu-20Ni-20Mn infiltrant. When the liquid infiltrant solidifies, it shrinks and leaves behind cavities. Some of these cavities get trapped and become pores within the infiltrant. In order to prevent these shrinkage pores from forming, the infiltrant must be solidified slowly and directionally such that the remaining liquid can always feed solidifying regions.

5.2.4 Corrosion issues

Mo is known to oxidize at high temperatures. This is a cause for concern and must be looked into. Oxidation of Mo at higher temperatures could deteriorate the wetting properties and hinder the infiltration process. The oxidation can be prevented by using a highly reducing atmosphere like hydrogen. Hence the infiltration should be carried out under hydrogen. The stability of the Mo oxide was calculated from the data in Appendix 8 [22]. An Ellingham diagram was constructed and is included in Figure 5-9 (a). It is more useful at higher temperatures, where the rates of most chemical reactions are much higher. It can be inferred from the diagram that the Mo oxides are more stable than those of Cu and Ni, however they are less stable than those of Mn. This inference can be made by calculating the P_{O2} in equilibrium with the oxide. The lower the value of P_{O2}, the more stable the oxide and the greater the tendency to form the oxide. Another inference is that Mo and Fe have around the same tendency to form oxides. Since the oxidation of the 420 stainless steel has been prevented at infiltration temperatures by using hydrogen, the same should occur for Mo. In the 420, the element with the greatest tendency to oxidize was Cr. It has a much greater tendency to oxidize than does Mo.

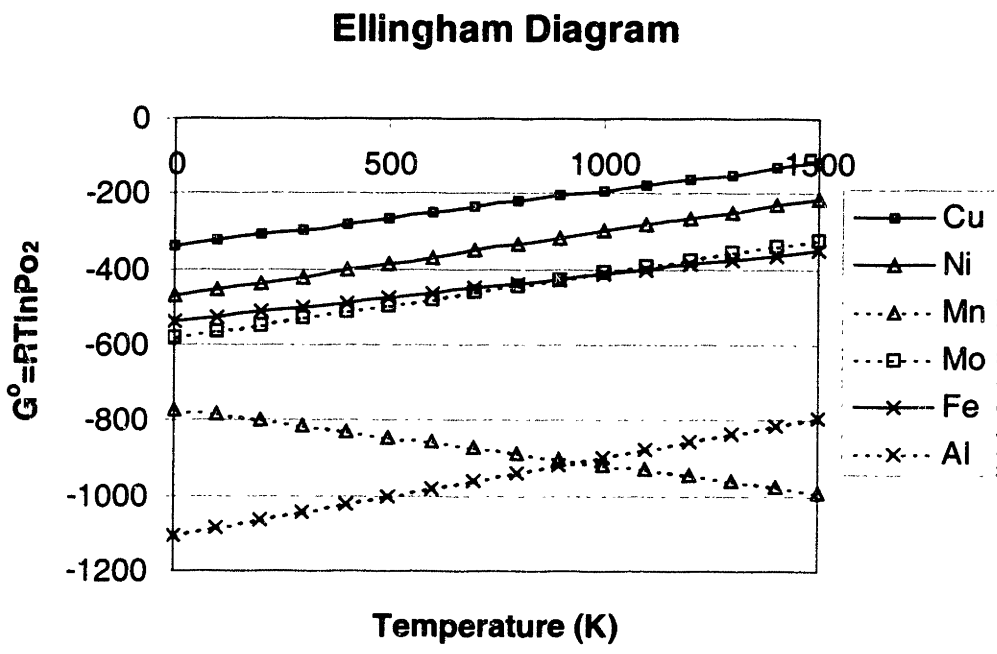

Figure 5-9 (a) : Ellingham diagram for Mo,Cu,Ni,Mn,Fe,Al

In the Mo/Cu-Ni-Mn system, the Mn will have a great tendency to oxidize, comparable to Cr in the 420/bronze system. The critical P_{O2} can be calculated from the Ellingham diagram, in order to prevent oxidation of Mn.

The electronegativity data in Appendix 8 also shows that Mo is more noble compared to Fe. It has a lower oxidation potential or a higher reduction potential. Hence it has a greater tendency to remain in an elemental form as compared to iron. The reduction reaction for both would be that of Cu with a half cell potential of +0.342 V. The oxidation of Mo has a potential of +0,2 V while that of Cr in the 420 is +0.744. Hence the cell potential for the 420/bronze system is a lot more than that of the Mo/Cu-Ni-Mn system.

The thermodynamic tendency for copper corrosion is low, as measured by a low free energy of chemical reaction with aqueous solutions and relatively noble potentials in the emf series. Thus copper and its alloys are quite corrosion resistant in many atmospheric and non oxidizing aqueous environments. Cu-Ni alloys are the most corrosion resistant of

all the Cu alloys [23]. Both Cu and Ni have excellent corrosion resistance to non oxidizing acids and find use in chemical process industries. These alloys show excellent stress corrosion cracking behavior. However, the presence of Mn could have a detrimental effect on the corrosion resistance of the Cu-Ni-Mn alloy [23].

Mo is added in certain Ni based alloys such as "Hastealloys" which are heat resistant and corrosion resistant to chemical solutions. On the other hand martensitic steels like 420 have a corrosion resistance which is lower than the other grades of stainless steel and applications are generally limited to mild environments. Because of high strength levels the 420 steel is susceptible to hydrogen induced cracking (HIC) [23]. Mo on the other hand is refractory in nature and has been found to less susceptible to HIC [23].

5.3 Experimental studies

5.3.1 Infiltrating coupons

Several experiments were conducted to study the infiltration of the Mo skeleton with a Cu-Ni-Mn infiltrant. Figure 5-9 (b) shows the basic experimental set up for the tests. Sintered Mo coupons were placed on a sintered Mo stilt within a ceramic crucible. Cu-Ni-Mn infiltrant chunks was placed around the stilt in the crucible. When the temperature surpassed the melting point of the infiltrant, the liquid infiltrant melted and flowed upwards through the stilt and into the part, driven by the capillary force existing due to the pore structure within the part.

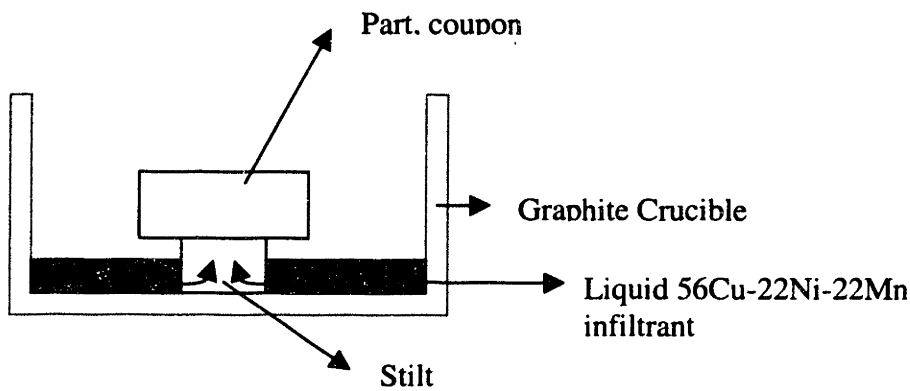

Figure 5-9 (b) : Infiltration of a Mo part or coupon with 56Cu-22Ni-22Mn infiltrant.

The infiltration tests were carried out in the MRF high-temperature furnace under several atmospheres, mainly forming gas and hydrogen. Infiltration temperatures and times were also varied. Since the liquidus of the infiltrant is 1060 °C, the minimum infiltration temperature is 1100 °C (at least 40 °C above the liquidus) and the maximum infiltration temperature is limited by the furnace capability, which is 1200 °C. The infiltration times were varied from ½ hour to 1 hour. The actual infiltration has been measured to be very rapid in the past and is expected to last only a couple of minutes. The infiltration time also depends on the size of the sintered part. These tests were conducted in the MRF high-temperature furnace and the tube furnace.

The results from these experiments are summarized in Table 5-1. The composition of the infiltrant was measured to be 56Cu-22Ni-22Mn in atom percent. The wetting behavior is generally better in hydrogen as compared to a forming gas atmosphere. The wetting behavior also seems to improve with an increase in temperature. This behavior is very consistent with the observations from earlier work [19]. In a forming gas atmosphere, the 56Cu-22Ni-22Mn infiltrant failed to infiltrate the porous compact at 1100 °C even though it displayed acceptable wetting properties. This has also been observed by other researchers [13]. Two possible causes for this poor infiltration have been postulated [13]. The first possibility was the formation of thin oxide layer/skin on the liquid infiltrant or

Mo powder that formed a physical barrier that had to be overcome. This film could be thinner at higher temperatures due to a less viscous infiltrant or a higher propensity for the oxides to be reduced by the forming gas. The second cause may be due a rise in the melting point of the infiltrant front as a result of reaction with the Mo skeleton. The second cause has been proven invalid by microprobe studies, which show no detectable amount of Mo in the infiltrated regions. The infiltration studies showed better infiltration under hydrogen gas atmosphere. This might be due to the fact that the hydrogen atmosphere was able to reduce any oxide skin formed on the infiltrant front or the Mo powder. The reducing nature of the hydrogen gas enabled better wetting and infiltration at all temperatures. This has also been observed in the past by researchers [19].

Infiltration Temperature	Infiltration Atmosphere	Wetting	Infiltration	Porosity
1100°C	Forming Gas	Fair	Poor	-
1100°C	H_2	Good	Fair	-
1150°C	Forming Gas	Fair	Fair	3%
1150°C	H_2	Good	Good	2%
1200°C	Forming Gas	Good	Fair	2%
1200°C	H_2	Good	Good	~0%

Table 5-1 : Results from the infiltration of a Mo skeleton with 56Cu-22Ni-22Mn infiltrant.

5.3.2 Porosity measurements

Experiments were conducted in order to measure the porosity in the infiltrated samples. Samples were cut, mounted and polished. An optical microscope was used to measure the porosity. For randomly distributed pores, the point fraction of the pores is identically equal to the volume fraction. The approximate amount of porosity was measured by the point counting method. A rectangular grid was placed over the microstructure and the fraction of intersections lying over porosity was measured and expressed as a percentage. It was used as a measure of porosity in the sample. Table 5-1 shows the effect of infiltration temperature and atmosphere on porosity. The hydrogen atmosphere seemed to work well in reducing porosity. This might be due to the fact that the wetting improves under hydrogen atmosphere. Figures 5-10 and 5-11 show the microstructures after infiltration under hydrogen atmosphere and forming gas. The porosity also appeared to

decrease at higher temperatures. The reduced viscosity of infiltrant at higher temperatures might be responsible for this behavior. The porosity appears to be non existent in the specimen infiltrated in hydrogen at 1200 °C.

Leakage tests were also carried out to determine the existence of any micro-porosity. Holes (3 mm in diameter) were drilled in a printed sample. This sample was then sintered and infiltrated. The sintering was done at 1200 °C for 12 hours in forming gas and the infiltration was also carried out at 1200 °C for 1 hour in hydrogen. Figure 5-12 shows the sample that was used for the leakage tests. After infiltration, the holes were filled with soap solution and air was blown through one hole at a time. There was no bubbling from other neighboring holes. Although this tended to indicate that there was no connectivity between the holes due to micro-porosity, later tests on tools with cooling channels showed leaking of the tool from the cooling channels to the surface. Initially, the reason for the leaking in the 420/bronze tools was thought to be due to the wide solidification range for bronze. However, the solidification range for the Cu-Ni-Mn alloy is only 1040°C-1060 °C. Hence another reason for the leaking was proposed which was the solidification shrinkage of the infiltrant alloy. As discussed earlier, this could potentially lead to connected porosity. An infiltration of the same tool was carried out under vacuum still resulted in leaking. This supported the new theory that the connected porosity was due to shrinkage voids instead of gas porosity.

Another feature observed after infiltrating in hydrogen was the presence of large gas voids (~1cm in diameter) at the base of the excess infiltrant. This was first thought to be due to the solubility mismatch of hydrogen gas in liquid and solid infiltrant. However it was finally proved that there was a reaction between the liquid Cu-Ni-Mn and the alumina plate beneath it resulting in the formation of a green manganese oxide and the evolution of a gas which possibly could be oxygen. The most probable reaction is that the liquid Mn might be reducing the alumina and forming an oxide itself. Figure 5-9 (a) shows that at 1200 oC the manganese oxide is more stable than the aluminum oxide. An infiltration in hydrogen was carried out with only BN as the substrate. No such porosity was observed at the base of the excess infiltrant.

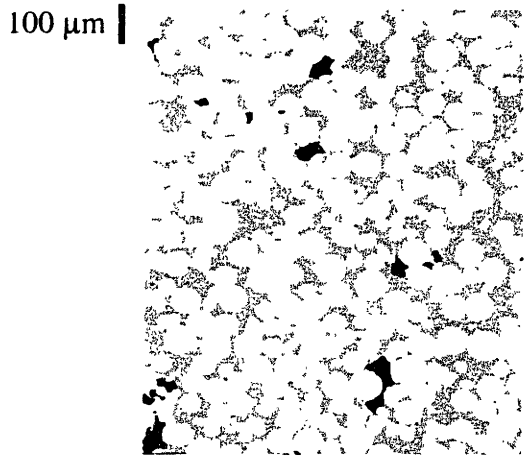

Figure 5-10 : Microstructure of Mo/56Cu-22Ni-22Mn infiltrated at 1200 °C for 1 hour under forming gas atmosphere.

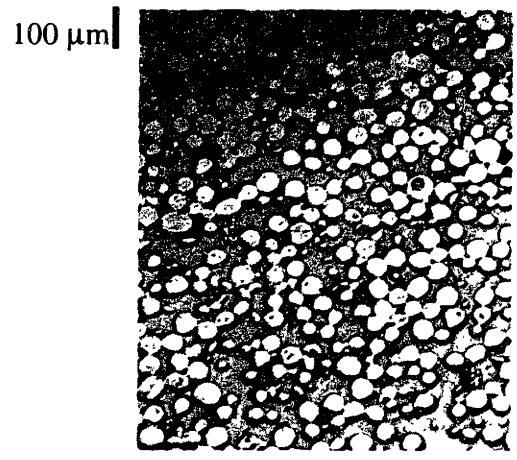

Figure 5-11 : Microstructure of Mo/56Cu-22Ni-22Mn infiltrated at 1200 °C for 1 hour under hydrogen gas atmosphere.

However one observation was that all the tools leaked from the bottom surface and not the top surfaces. An explanation was put forward for this. It had to so with the moving of liquid fronts in the tool during infiltration. During the sectioning of one such tool small gaps were observed between the surfaces of the tool and the stilt. These gaps could result in the separate infiltrant fronts travelling into the tool and then joining inside the tool. If the joining is not perfect then a path could exist between the cooling channels and the bottom surface of the tool. This could be solved by printing the stilt onto the part.

5.3.3 Reaction between Mo and the infiltrant (Microprobe studies)

Experiments were also carried out to study the reaction between the skeleton and the infiltrant. The sample from the infiltrated specimen was mounted, polished and examined using scanning electron microscopy. Figure 5-13 shows the micrograph of the Mo particle and the Cu-Ni-Mn infiltrant. The uneven nature of the Mo powder surface suggested that some Mo might be dissolving. A composition trace was done from the middle of the particle to a remote point in the infiltrant region. Figure 5-14 and Table 5-2 show the results obtained from the compositional trace. There is minimal reactivity between Mo and the infiltrant. Only about 1 at.% Cu was found to be in solution with the

Mo powder with an even lesser amount of Ni and Mn present. This is consistent with the results obtained from the Thermo-Calc study which showed minimal reaction between the Mo particle and the infiltrant (1% Cu in solution with solid Mo). The microprobe studies showed no Mo in the infiltrant. The uneven nature of the Mo surface still remains puzzling.

However one other observation is worth noting. Some of the Mo particles at the edge of the part had apparently dissolved and resolidified. This could be due to the increase in the solubility of Mo at higher temperatures. It might also have to do with the hydrogen gas atmosphere in which the infiltration was carried out. Fig 5-15 shows the observed phenomenon.

	Nickel	Copper	Manganese	Molybdenum
Bulk Infiltrant Region	22.9	54.66	22.4	0.04
Interface of infiltrant / particle	20.3	59.11	20.5	0.09
1 micron into a Mo powder particle	0.6	1.7	0.5	97.2

Table 5-2 : Elemental composition in at.% across the Mo particle/56Cu-22Ni-22Mn infiltrant interface.

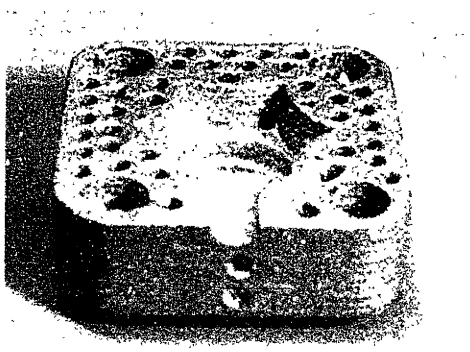

Figure 5-12 : Infiltrated Mo/56Cu-22Ni-22Mn part used for leakage testing.

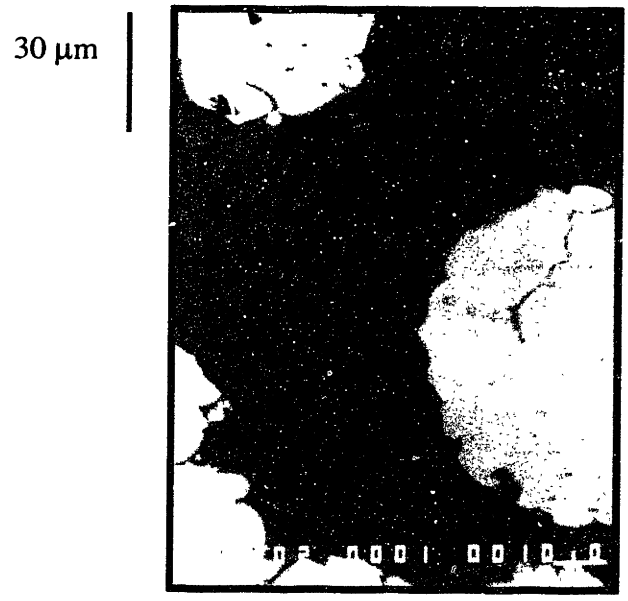

Figure 5-13 : Microstructure of Mo/56Cu-22Ni-22Mn infiltrated at 1200 °C for 1 hour

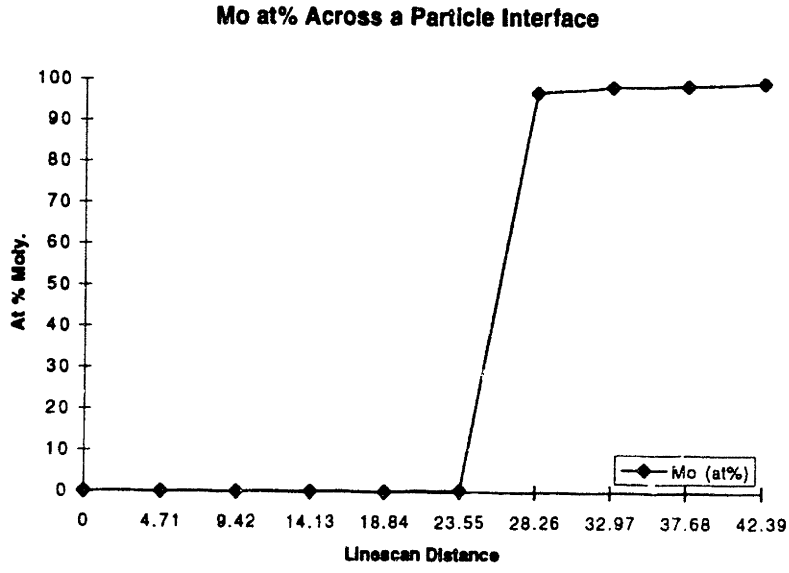

Figure 5-14 : Composition of Mo in at.% across the Mo particle/56Cu-22Ni-22Mn infiltrant interface. (Linescan distance is in microns)

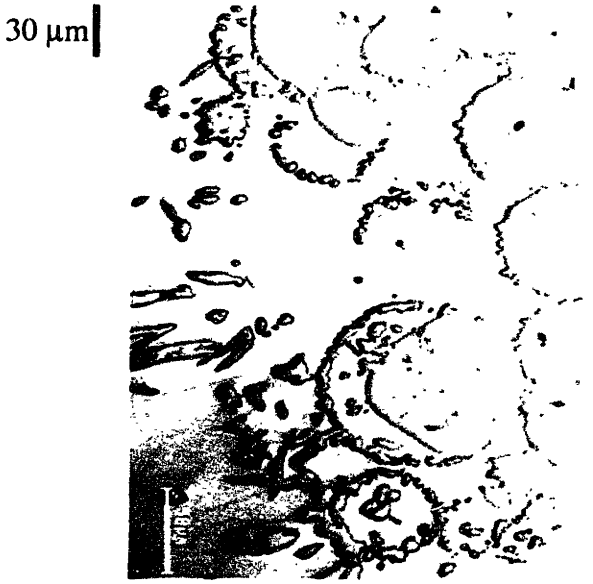

Figure 5-15 : The break up of the Mo particle observed at the edge of the part during infiltration under H_2 gas.

5.3.4 Dimensional changes

Dimensional changes that occur during infiltration were also measured using vernier calipers. There was a shrinkage of approximately 0.2 % observed during the optimal infiltration treatment (see following section). This could have resulted from reaction between the Mo particle and the infiltrant but microprobe analysis showed such reactions to be minimal. The only possible explanation might be the fact that re-arrangement of the Mo particles occurs during infiltration, leading to particles coming closer together and causing shrinkage. Another possibility is that some liquid-phase sintering might be occurring and causing the Mo particles to come close together. As mentioned earlier, one of the concerns was the slumping of the part during the infiltration. This was however not observed.

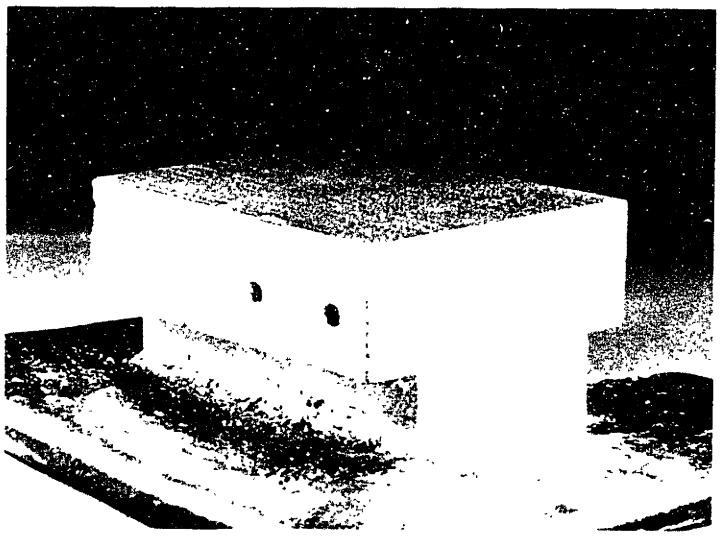

Figure 5-16 : Mo/56Cu-22Ni-22Mn tool with conformal cooling channels.

5.4 Optimal infiltration treatment

An optimal infiltration treatment was developed for the alloy system. The details are included in Appendix 3. The infiltration temperature is 1200 °C and the infiltration time is 45 minutes. An infiltration temperature of 1200 °C was chosen in order to achieve good wetting of the Mo skeleton and minimum porosity in the infiltrated part. A higher temperature would result in a higher solubility of the Mo skeleton in the 56Cu-22Ni-22Mn infiltrant. The atmosphere is hydrogen, which does add complexity to the heat treatment process. The use of hydrogen requires extra precautionary measures due to the explosive nature of the gas. All hydrogen infiltration was carried out in the high temperature MRF furnace.

Some Mo/56Cu-22Ni-22Mn tools with conformal cooling channels were manufactured for Motorola using the optimal infiltration treatment. One such tool is shown in Figure 5-16. Note the stilt which supports the tool and the excess infiltrant surrounding the stilt. Appendix 9 gives the dimensional changes that were observed on the tools during infiltration. The shrinkage in the tools was around 0.5 % which is greater than that observed on the coupons.

6 Age Hardening of Cu-Ni-Mn

6.1 Principle of age hardening

Age hardening also known as precipitation hardening is produced by solution treating and quenching an alloy in which a second phase is in solid solution at the elevated temperature but precipitates upon quenching and aging at a lower temperature [24]. For age hardening to occur, the second phase must be soluble at an elevated temperature but must exhibit decreasing solubility with decreasing temperature. In age hardening systems there is generally some degree of atomic matching, or coherency, between the lattices of the precipitate and the matrix. The requirement of a decreasing solubility with temperature places a limitation on the number of useful age-hardening alloy systems. The common age hardening alloy systems are aluminum, nickel and copper alloys. One such age hardening alloy is Cu-Ni-Mn.

The age hardening treatment comprises of a solution treatment and an aging treatment. The solution treatment is at a higher temperature where the second phase is completely soluble. The aging treatment is at a lower temperature where the second phase is stable and it precipitates out of solution.

6.2 Cu-Ni-Mn, phase equilibria

The alloy Cu-Ni-Mn has been successfully used as an age hardenable alloy in the past. Several studies have been done on the age hardening characteristics of the alloy. Although several variations in compositions exist, they are small and the general composition of all commercial age hardening grades is 60 at.% Cu, 20 at.% Ni and 20 at.% Mn.

6.2.1 Study of the various binary and ternary systems

6.2.1.1 Binary systems

The binary and ternary systems for this alloy have been extensively studied in the past. The phase diagram for the Cu-Mn system is given in Figure 6-1 [18]. According to the reviews, a peritectic reaction L+δ = γ occurs at 1098 °C. The phase diagram shows a large solubility of Mn in Cu and vice versa. The solid solution is the γ phase. This phase has a melting point minimum at 887 °C.

The Ni-Mn phase diagram has also been studied extensively in the past. Recently, it was calculated using Thermo-Calc software and is included in Figure 6-2 [25]. The γ phase is the stable high temperature phase with a melting point minimum of 1018 °C. The crystal structure for the γ phase is face centered cubic (fcc). At lower temperatures, an equiatomic MnNi phase stabilizes. Chang proposed that this phase has a $L1_0$ structure. It is an ordered phase with a very high hardness. An effort was made to estimate the L_1 and L_0 parameters in the regular solution model for Ni and Mn in order to get a $L1_0$ phase region for the NiMn precipitate (Figure 6-2) [25]. The results agreed well with earlier studies [26,27,28].

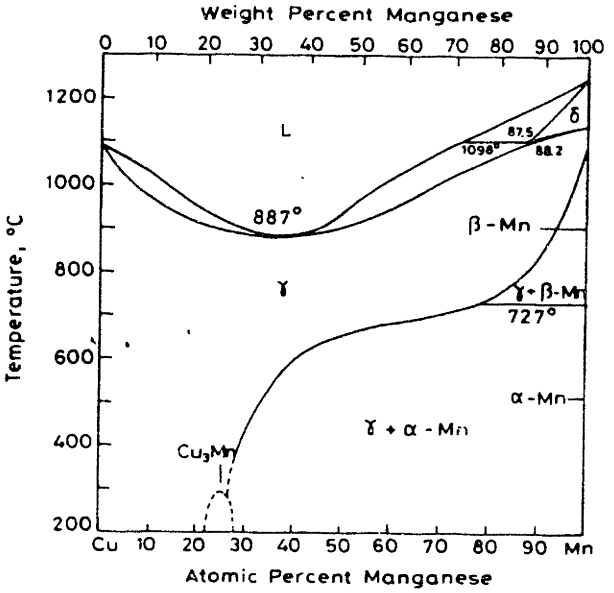

Figure 6-1 : The Cu-Mn phase diagram.

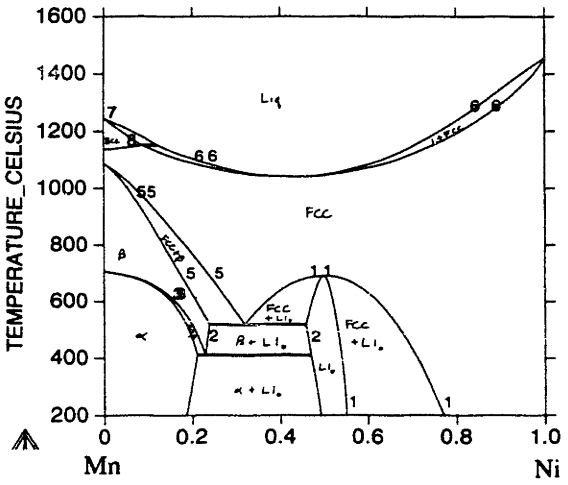

Figure 6-2 : The Ni-Mn phase diagram.

The Cu-Ni phase diagram was also calculated and is shown in Figure 6-3 [25]. This diagram is very simple. There is a low temperature miscibility gap that peaks at 65 at.% Ni and 450 °C. The stable phase at high temperatures is the γ phase and it has a fcc structure.

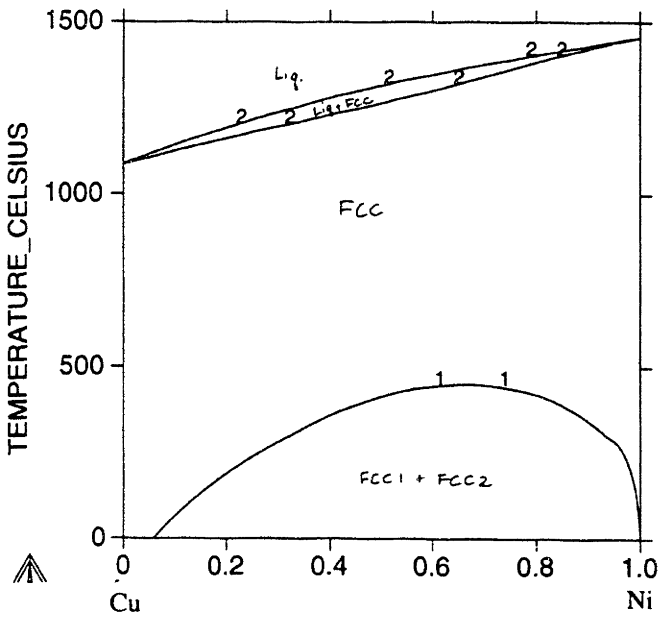

Figure 6-3 : The Cu-Ni phase diagram.

6.2.1.2 Ternary system

A room temperature isotherm was calculated for the Cu-Ni-Mn system in 1941 [29]. It is shown in Figure 6-4. Except for the miscibility gap in Cu-Ni, which is missing, the diagram is very accurate. Researchers have developed liquidus and solidus isotherms for the Cu-Ni-Mn system [20]. The solidus isotherm is shown in Figure 6-5. The first melting starts at 887°C,which is the solidus minimum for the Cu-Mn system. As the temperature rises the solidus moves towards higher Ni compositions. The composition in question (60Cu,20Ni,20Mn) has a solidus temperature between 1000 °C and 1100 °C, somewhere around 1040 °C. The liquidus isotherms for the system are shown in Figure 6-6. The liquidus temperature for the age hardening alloy (60Cu-20Mn-20Ni) is around 1070 °C, above which the alloy is 100 percent liquid. The solidus and liquidus isotherms also depict that a small change (~5 %) in at.% Cu in the infiltrant does not change the liquidus and solidus temperatures appreciably as long as the Ni and Mn are in equal at.%.

An isopleth for equal atomic fractions of Mn and Ni was calculated for the Cu-NiMn system [26,27,28]. (Figure 6-7) It can be seen that for pure Cu, the γ phase is the only solid stable phase over all temperatures. As the atomic percent of Mn and Ni increase equally, a second phase becomes stable at lower temperatures. This is the NiMn phase with an $L1_0$ configuration. Also, the critical temperature, below which this phase is stable, increases as the concentration of Ni and Mn increases. At 20 at.% Ni and Mn, the critical temperature is around 510 °C. Therefore, this is material system is an ideal candidate for an age hardening system due to the presence of a second phase (NiMn) which dissolves at an elevated temperature and is stable at lower temperatures.

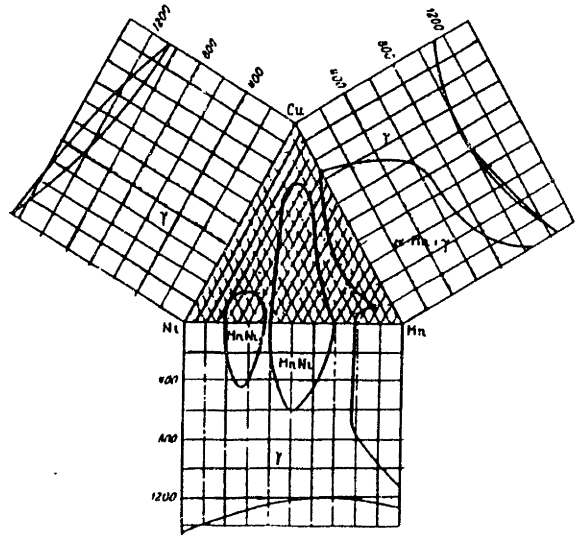

Figure 6-4 : Room temperature isotherm for Cu-Ni-Mn.[29]

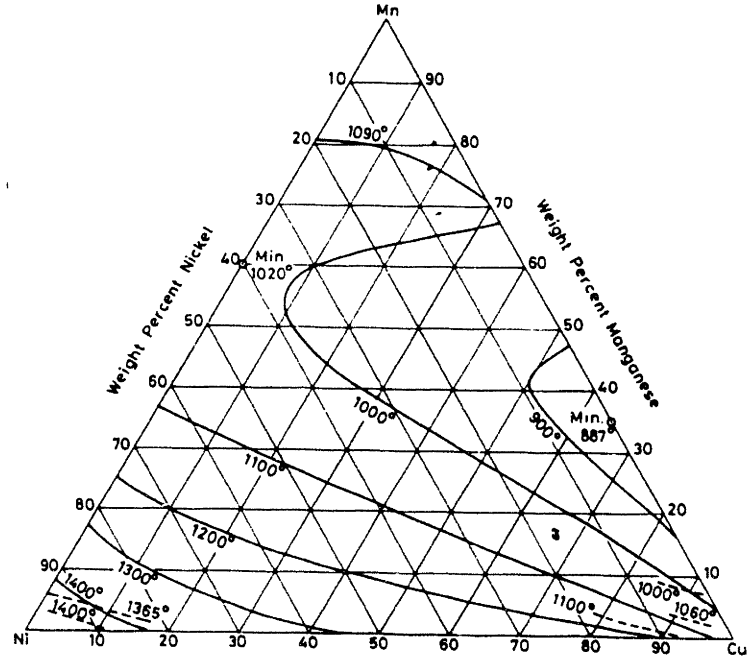

Figure 6-5 : Solidus isotherm for Cu-Ni-Mn.[20]

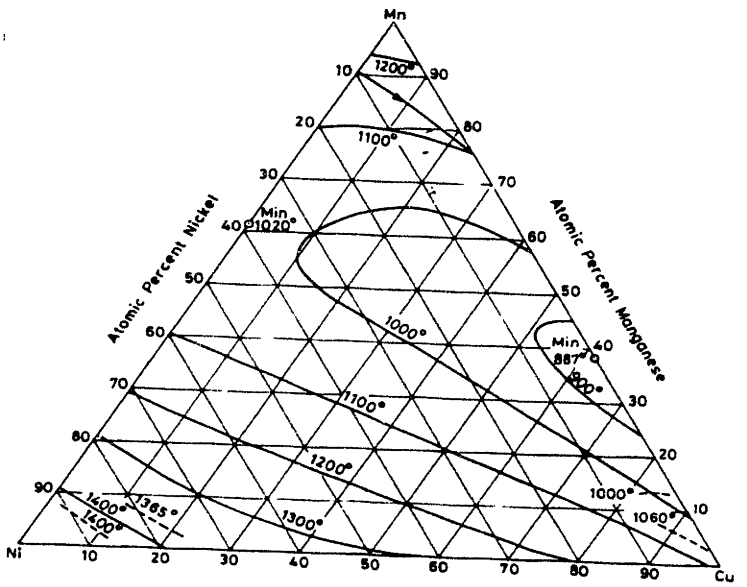

Figure 6-6 : Liquidus isotherm for Cu-Ni-Mn.[20]

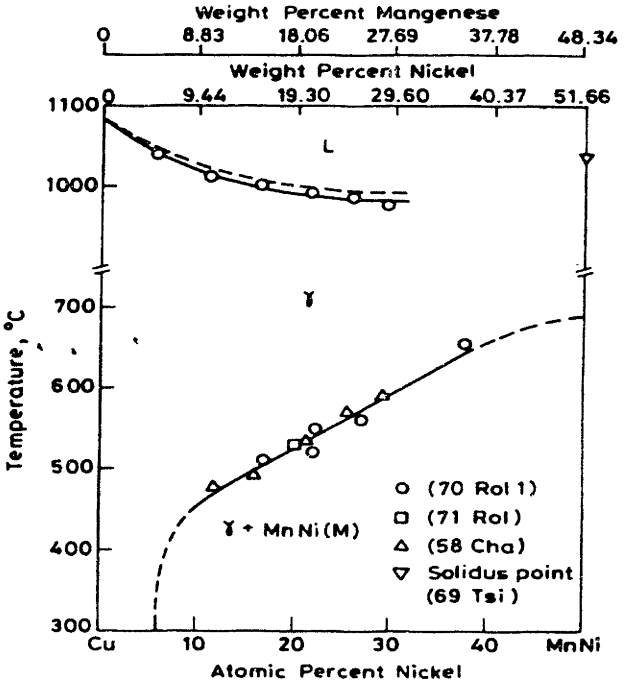

Figure 6-7 : Isopleth for Cu-Ni-Mn having equi-atomic fractions of Ni and Mn. [26,27,28]

6.2.2 Age hardening behavior of Cu-Ni-Mn

The age hardening response of Cu-Ni-Mn is well studied [29]. Several alloys were tested with compositions varying from 22 to 24 at.% Ni and Mn. The aging temperature was varied from 350 °C to 450 °C and the aging time was varied from 4 to 24 hours. The aging treatment was preceded by cold working or solution treatment. The solution temperature before aging was varied from 900 °C to 650 °C with a time of 1 hour. All the aging was carried out in an inert (Ar) atmosphere. The results showed that solution treatment at 650 °C for 1 hour followed by aging at 350 to 450 °C produces the maximum hardness. A higher solution treatment leads to unnecessary grain growth, which results in a loss in hardness and ductility. The hardness increased with time of aging and the over-aging time was around a week. For aging times greater than this time, a reduction in hardness was observed. The rate of increase in hardness was initially high and became very small after 24 to 48 hrs of aging time. The aging times and temperature could be manipulated in order to get a desired hardness level. Figures 6-8 to 6-10 illustrate the hardness vs. time curves for the various alloys tested. The solution treatment for all the alloy grades was 650 °C for 1 hour. Several conclusions can be made after studying the plots more carefully:

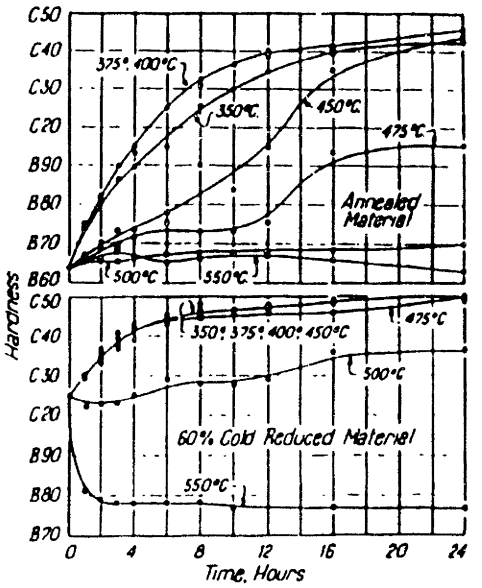

Figure 6-8 : Hardness versus time plot for the aging of 60Cu-20Ni-20Mn.[29]

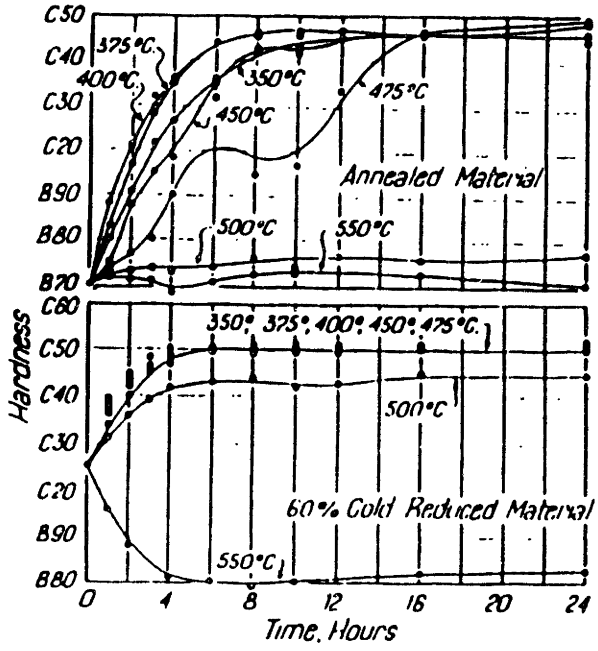

Figure 6-9 : Hardness versus time plot for the aging of 56Cu-22Ni-22Mn.[29]

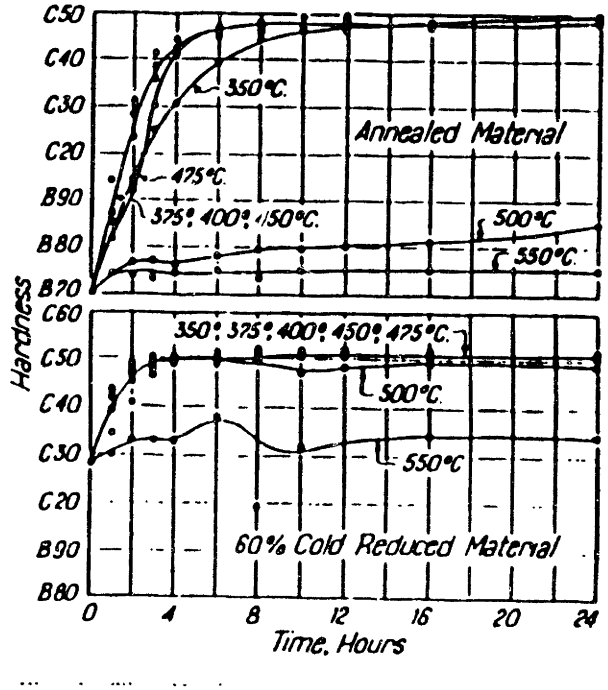

Figure 6-10 : Hardness versus time plot for the aging of 52Cu-24Ni-24Mn.[29]

The hardening rate is a lot higher for the cold worked material vs. the solution treated material. The Mn and Ni content does influence the initial rate of hardening but has little effect on the final hardness attained at high times (>24 hours). Higher amounts of Ni and Mn result in higher initial hardening rates. The aging temperatures between 350 °C and 450 °C show good hardening. The aging time is critical initially but then becomes irrelevant at higher times (>24 hours). The maximum hardness achieved for the optimal aging temperatures is slightly below 50 Rc.

Microscopic examination of the hardened alloys shows two different microstructures depending on the aging temperature. When aged at temperatures up to and including 400 °C, a finely divided precipitate appears in the grain boundary areas and this spreads gradually throughout the grains. The grains have been considerably altered in the process of precipitation. Aging at 450 °C and above produces a grain boundary phase that has little tendency to spread through the grains themselves. A change in electrical resistance with aging has also been observed [29]. The resistivity drops from 87 to 67 microhms per centimeter cube when the sample is aged from the solution treated state and from 88 to 63 microhms per centimeter cube when aged from the cold worked condition. This agrees with the metallographic evidence since precipitation should decrease the resistivity. This also might result in a better heat conductivity due to precipitation.

6.3 Experimental work with 56Cu-22Ni-22Mn

6.3.1 Heat treatment

The Cu-Ni-Mn alloy was obtained from Hasboro Corporation. The composition of the alloys varied only slightly. The average composition was 56 at.% Cu, 22 at.% Ni and 22 at.% Mn. Small coupons of the alloy were encapsulated in a test tube with an inert atmosphere (argon). The solution temperature was 650 °C for all the samples. The solution time was one hour. The samples were quenched in oil and then again aged at different temperatures for different times. Several aging treatments were conducted on

the encapsulated samples. The aging temperatures were 350 °C, 400 °C and 450 °C. The aging times were 12 hrs, 24hrs and 48 hrs.

	Aging Temperatures		
Times	**350 C**	**400 C**	**450 C**
12 hrs	67 Rb	77 Rb	95 Rb
24 hrs	80 Rb	22 Rc	27 Rc
48 hrs	-	-	35 Rc

Table 6-1 : Macro-hardness results from age hardening of 56Cu-22Ni-22Mn.

The hardness attained from these tests was well below that observed during earlier studies [29]. This brings up the issue whether the encapsulation is hindering age hardening by retarding the heat transfer perhaps by retarding the quenching rate.

6.3.2 Macro-hardness measurements

Table 6-1 shows the macro-hardness obtained after each of the treatments. A maximum hardness of 35 Rc (Rockwell C scale) was obtained in the sample that was aged at 450 °C for 48 hours. Each of the heat-treated samples were cut, mounted and polished. Macro-hardness readings were taken using a Rockwell testing machine. Table 6-1 shows the results obtained. For a given aging time, the hardness increases with the aging temperature. For a given aging temperature, the hardness increases with aging time. The as cast hardness before aging was 70 Rb (Rockwell B scale). The maximum hardness obtained after aging at 450 °C for 48 hours was 35 Rc.

6.3.3 Microstructure evaluation

In order to view the microstructure, the polished samples were etched with 5 mg. of $FeCl_3$, 20 ml of HCl and 100 ml of ethanol. Two different microstructures were observed depending on the aging temperatures (Figures 6-11and 6-12). When aged at 450 °C for 24 hours, the microstructure resembled that of spinodal decomposition but on a relatively coarse length scale. Microprobe analysis showed that the darker phase has an equal Ni and Mn composition and the lighter phase had a higher Mn concentration as compared to the Ni. The dark phase comprises of the NiMn precipitates. The precipitation starts at the

grain boundaries and spreads inwards. The microstructure of the sample aged at 400 °C showed precipitation mainly along the grain boundaries. This could be occuring because grain boundary diffusion might be dominating at 400 °C and volume diffusion might be dominating at 450 °C.

Figure 6-11 : Microstructure of 56Cu-22Ni-22Mn aged at 400 °C for 24 hours.

Figure 6-12 : Microstructure of 56Cu-22Ni-22Mn aged at 450 °C for 24 hours.

6.4 Experimental work with Mo/Cu-Ni-Mn

6.4.1 Heat treatment

Infiltrated Mo/Cu-Ni-Mn coupons and parts were subject to the optimal age hardening treatment observed in previous studies. The age hardening was done in a box furnace built at MIT [8]. The atmosphere was forming gas (95% argon + 5% hydrogen), and the oxygen content in the atmosphere was closely monitored in order to prevent oxidation of the part. The dew point was monitored using a dew point sensor and always kept below – 20 °C. The samples were solution treated at 650 °C for 1 hour and then furnace cooled to the aging temperature of 450 °C where they were held for 48 hours. The furnace cooling

rate was very critical and was experimentally measured to be 7 °C/min. A very slow cooling rate will cause the precipitation to occur before the aging temperature is reached. This will result in a lower hardness. The age hardening was done for samples consisting of 30 μm and 62 μm Mo powder.

6.4.2 Hardness measurement

The samples were prepared as described in section 6.3.2. Macro-hardness readings were taken using a Rockwell B indentor and a hardness testing machine. Micro-hardness readings of the Mo particles and the Cu-Ni-Mn infiltrant were also taken using the micro-hardness testing machine, Table 6-2 shows the values that were obtained for both the solution treatments using a 100g Vickers indentor. Direct conversion of these values to the Rockwell scale will give erroneous results for copper alloys such as Cu-Ni-Mn. Hence the hardness values are reported in a 100g Vickers scale (Hv). The Mo has a approximately constant hardness (~240 Hv) which is not affected by the aging treatment. The Cu-Ni-Mn infiltrant hardens from around 160 Hv to 470 Hv after the age hardening treatment. 470 Hv converts to around 47 Rc on the Rockwell C Scale. This is in agreement with the hardnesses obtained from earlier studies on Cu-Ni-Mn alloys [29]. The macro-hardness increases from 70 Rb to 99 Rb after the age hardening treatment. The macro-hardness obtained after age hardening is similar to that in the hardened 420/bronze system. However there is one big difference between the two systems. In the Mo/Cu-Ni-Mn system there is a smaller difference in the hardness between the skeleton and the infiltrant. In the 420/Bronze system this difference is much greater. The hardness obtained in the 420 steel phase (700 Hv) is still higher than that in the Cu-Ni-Mn infiltrant (470 Hv). However, that obtained in the Bronze infiltrant (220 Hv) is significantly lower than the Mo particle (250 Hv).

Again the effects of encapsulation are evident. The Mo/Cu-Ni-Mn samples that were encapsulated hardened to a lesser degree. Another observation is that the 30 μm Mo sampies seemed to harden exactly similar to the 62 μm Mo samples.

Material System	Heat Treatment	Mo powder	Cu-Mn-Ni infiltrant	Macro-hardness (Rb)
Mo(62μm)/Cu-Ni-Mn	Unaged	230	160	70
Mo(62μm)/Cu-Ni-Mn	solution: 650°C,1 hr aging: 450 °C,48 hrs, Ar atmosphere (encapsulated)	230	312	83
Mo(62μm)/Cu-Ni-Mn	solution: 650°C,2 hrs aging: 450 °C,48 hrs, Ar atmosphere (encapsulated)	224	281	84
Mo(62μm)/Cu-Ni-Mn	solution: 650 °C,1 hr aging: 450 °C,48 hrs, Forming gas atmosphere	250	476	99
Mo(30μm)/Cu-Ni-Mn	solution: 650 °C,1 hr aging: 450 °C,48 hrs, forming atmosphere	255	455	98
		420 powder	**Cu-10Sn infiltrant**	**Macro-hardness (Rb)**
420 ss/Cu-10Sn	as infiltrated (hardened)	700	225	100
420 ss/Cu-10Sn	annealed	273	220	77
420 ss/Cu-10Sn	quenched (re-hardened)	510	225	96

Table 6-2 : Hardness results (Vickers 100g load) from the age hardening tests on Mo/56Cu-22Ni-22Mn and comparison with the 420/Cu-10Sn system.

6.4.3 Microstructure evaluation

The microstructure of the infiltrated and age hardened specimen was observed using the JEOL SEM. The etchant used was again 5 mg of $FeCl_3$, 20 ml of HCl and 100 ml of ethanol. Fine precipitates, 1 μm in size were observed throughout the Cu-Ni-Mn phase. These precipitates were uniformly distributed. At higher magnifications, precipitation was observed on the surface of the Mo particles. Since the size of the precipitate (1 μm) is the same as the minimum beam diameter for the SEM, it was not possible to measure the composition of the precipitate. However they are expected to be precipitates of an

equi-atomic ordered NiMn phase. Figures 6-13 illustrates the microstructures that were observed. Elemental mapping results show no segregation on a macro-scale. The segregation occurs on the scale of the precipitates (~1 μm). This is too fine to be picked up by elemental mapping studies.

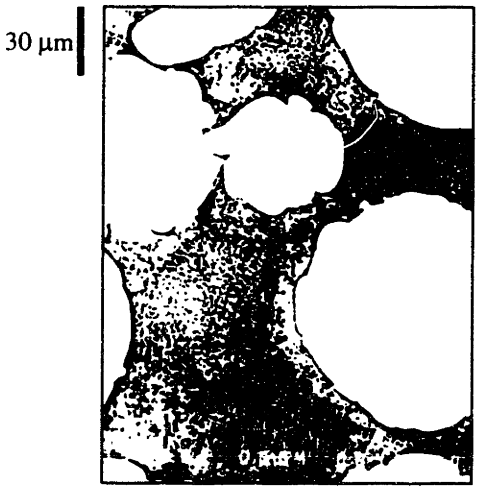

Figure 6-13 : Etched microstructure of Mo/56Cu-22Ni-22Mn aged at 450 °C for 48 hours.

6.4.4 Dimensional measurements

The dimensions of the part were monitored using Vernier calipers. There was no observed dimensional change or distortion resulting from the solution/age hardening heat treatment cycle. This is expected as age hardening treatment is not typically associated with significant distortion or dimensional changes.

6.5 Optimal age hardening treatment

Based on all the results obtained, an optimal age hardening treatment was developed for the Mo/Cu-Ni-Mn system. It is included in Appendix 3. It involves a solution treatment at 650 °C for 1 hour and an age hardening treatment at 450 °C for 48 hours in forming gas. The hardness of the 56Cu-22Ni-22Mn phase should be 47Rc or 470 vickers after age hardening. The macro-hardness obtained from the age hardening of Mo/56Cu-22Ni-

22Mn is comparable to that obtained in the 420/bronze system, which is around 20Rc or 100 Rb. Figure 6-14 shows an age hardened Mo/56Cu-22Ni-22Mn part. Very little oxidation was observed during the age hardening treatment.

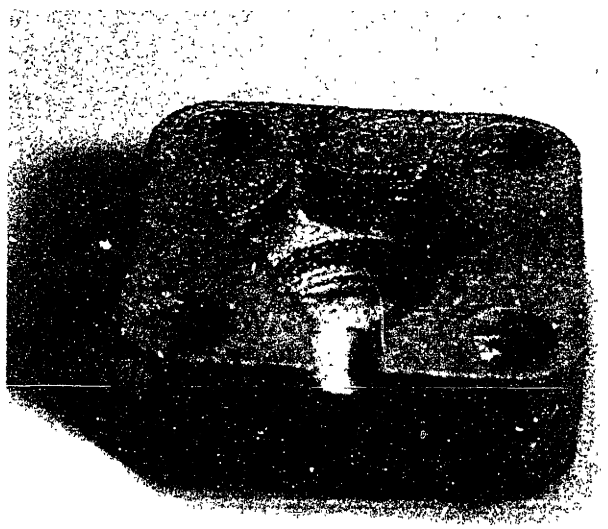

Figure 6-14 : Age hardened Mo/56Cu-22Ni-22Mn part.

7 Alternative Approaches to Developing a Hardenable System

7.1 Concerns with the Mo/Cu-Ni-Mn system

A major concern with the Mo/Cu-Ni-Mn is the electro-discharge machining (EDM) performance. Several EDM tests were done on the material at Extrude Hone, Irwin, PA. The results showed substantial electrode wear mainly due to the high melting point of Mo. However some later work performed at Motorola indicated that the wire EDM cutting rates of Mo/Cu-Ni-Mn are similar to those of tool steels.

Another potential concern is the weight of the part. Due to the high density of Mo (10.22 g/cm^3) as compared to stainless steel (~$8g/cm^3$), the weight of parts made from Mo powder is about 25% higher. This could potentially lead to problems such as slumping during infiltration. This was however not observed during the infiltration experiments.

The oxidation of Mn was also a potential concern. A small amount of oxidation was observed during the aging treatment. This could be due to the presence of trace oxygen in the furnace which caused Mn to oxidize.

The high melting point and density are due to the refractory nature of Mo. In order to improve the EDM performance and reduce the weight of the part, a non-refractory metal powder will be required.

7.2 Alternative powders

.One possible solution for improved EDM performance was to use a different metal powder with the Cu-Ni-Mn infiltrant. An experiment was carried out to determine the interaction of several possible metallic candidates with the Cu-Ni-Mn infiltrant (Figure 7-

1). A small chunk of infiltrant was placed on thin plates of Co, W, Ta, Ni, V, Mo and Fe. The sample array was heated to 1200 °C and held for 1 hour. The results are summarized in Table 7-1. The only metals that wetted well and did not dissolve were Mo, W and Ta. Because W and Ta are refractory metals with a higher melting point, they are expected to have EDM performance that is inferior to Mo. The other elements tested would not be useful as powders because of the excessive reaction with the Cu-Ni-Mn infiltrant.

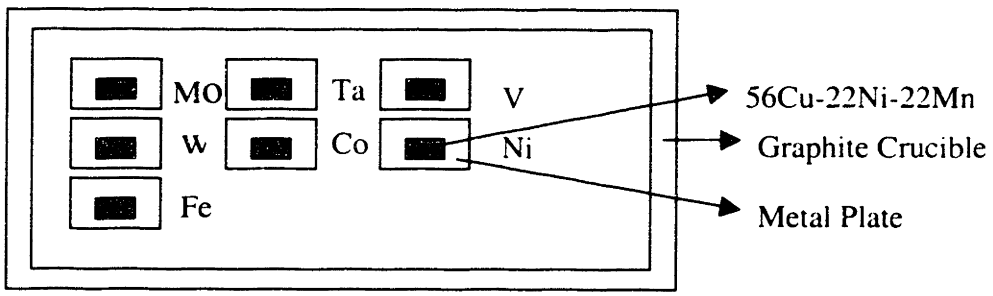

Figure 7-1 : Reaction between several metals and 56Cu-22Ni-22Mn

Metal	Crystal Structure	Wetting	Dissolves
Co	hcp	good	yes
W	bcc	good	no
Ta	bcc	good	no
Ni	fcc	good	yes
Fe	bcc & fcc	good	yes
Mo	bcc	good	no
V	bcc	poor	no

Table 7-1 : Summary reaction between 56Cu-22Ni-22Mn and several metals.

7.3 Coatings on powders

An optimum materials system for 3DP tooling would be one in which a non-refractory metal powder (like 420 stainless steel) could be used along with the Cu-Ni-Mn infiltrant. However, the previous experiment showed that the Cu-Ni-Mn would dissolve a good portion of the 420 stainless steel skeleton. One way to stop this reaction is to coat the 420

stainless steel powder with a diffusion barrier. This barrier could be a metallic or ceramic coating. In the past TiC has been successfully coated on steel and has been used mainly as diffusion barriers. A series of experiments were done to study the behavior of TiC coatings on steels. They are described in detail in the next section.

7.3.1 Experimental work

7.3.1.1 Immersion tests

Several different grades of tool steel bars were acquired and cut into small discs, 1 inch in diameter. The different grades and their elemental compositions are illustrated in Table 7-2. One of the side faces of the disc was turned and the other face was ground. They were then coated with a single layer of TiC by chemical vapour deposition at Toll Coating Services. Coating thicknesses of approximately 1 μm, 2 μm and 3 μm were used. One disc of every tool steel grade (6 in all) was placed in an alumina crucible (Figure 7-2) and supported by a Mo rod that ran through the center. Chunks of Cu-Ni-Mn infiltrant were also placed in the crucible. The entire set up was heated to 1200 °C for 1 hour in the high-temperature MRF furnace, under forming gas atmosphere. The infiltrant melted and flowed around the discs, completely wetting them and adhering to them. The sample array was the furnace cooled to room temperature.

Grade	C	S	P	Si	Mn	Cr	Ni	Mo	V	W	Nb
M2	0.85	-	-	0.3	0.3	4	0.3	5	2	6	-
M4	1.3	-	-	0.3	0.3	4	0.3	4.5	4	5.5	-
D2	1.5	-	-	-	0.6	12	0.3	1	1	-	-
H13	0.35	-	-	1.2	0.5	5	0.3	1.5	1	-	-
440C	1	0.03	0.04	1	1	17	-	0.75	-	-	-
174PH	0.07	0.03	0.04	1	1	16	3-5	-	-	-	0.3

Table 7-2 : Compositions of different tool steels (wt.%).

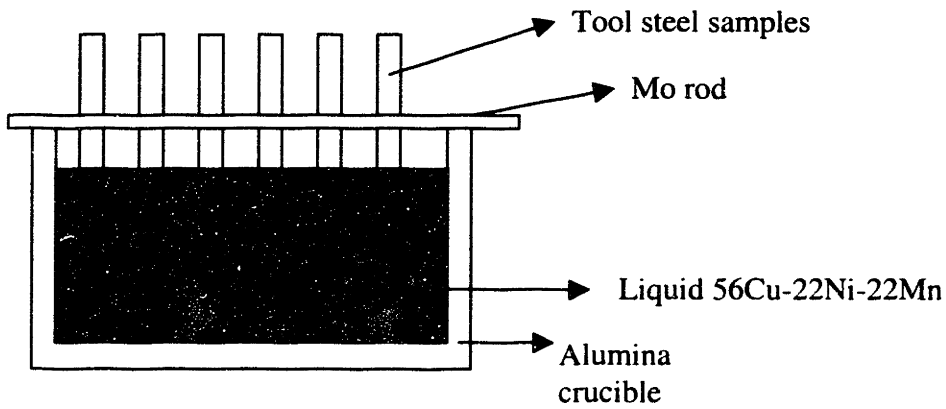

Figure 7-2 : Immersion of tool steel samples in 56Cu-22Ni-22Mn.

7.3.1.2 Microscopic examination

After heat treatment, small specimens including the tool steel-infiltrant interface were cut, mounted and polished. The microstructures were viewed under the SEM (Figures 7-3). The Cu-Ni-Mn infiltrant appeared to have penetrated the TiC coating into steel phase. Microprobe studies confirmed the presence of Cu, Ni and Mn under the TiC coating. There was also Fe present in the bulk infiltrant. There were two possible explanations for this behavior. The first was that the infiltrant had diffused through the coating. However, the diffusion data included in Appendix 7 indicate that the diffusivities of metallic elements through TiC are around 10^{-16} cm^2/sec. A crude calculation (see Appendix 7) indicates that the diffusivity of the elements through the TiC layer would have to be at least 10^{-9} cm^2/sec to achieve the observed penetration of 60 μm. This suggests that the infiltrant did not diffuse through the TiC layer.

The second possibility is that the coating developed several defects through which the infiltrant penetrated into the steel phase. This is more plausible and was actually observed in the microstructures. Small breaks in the coating were observed through which the infiltrant penetrated.

Another observation was that the infiltrant penetrated the coating only in those areas where the coating was adherent to the steel. There were certain areas where the coating

did not adhere to the steel particle. The infiltrant did not penetrate the coating in these areas (Figure 7-4).

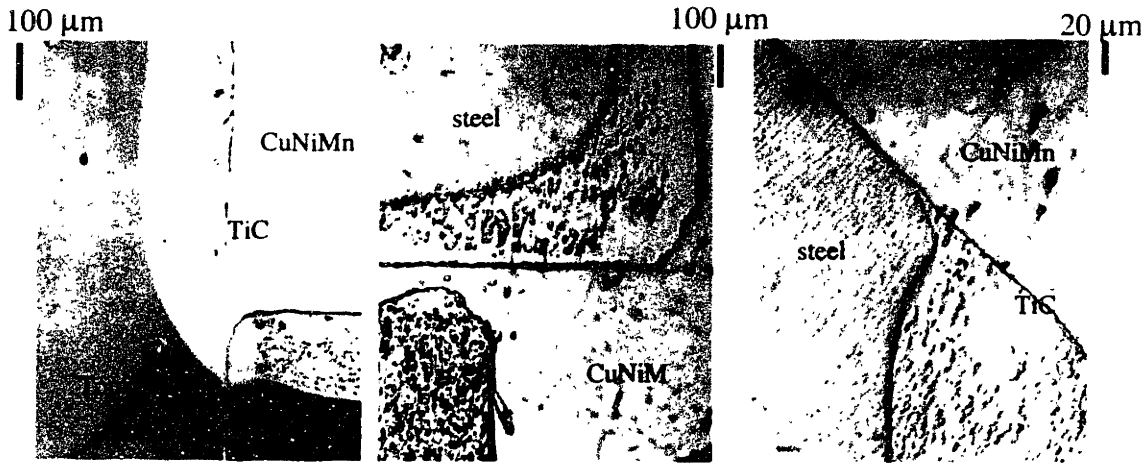

Figure 7-3 : Microstructures of TiC coated tool steel wetted by 56Cu-22Ni-22Mn indicating penetration.

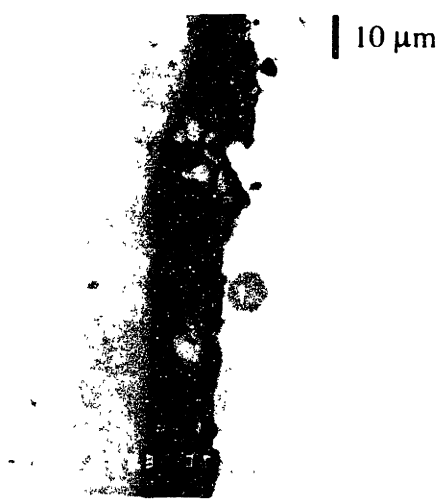

Figure 7-4 : Microstructure of TiC coated tool steel wetted by 56Cu-22Ni-22Mn showing no penetration.

7.3.2 Possible causes for the failure of the coating

The failure of the TiC coating could be due to several reasons. A thickness of 3 μm is large enough for large stresses to develop as a result of coefficient of thermal expansion (CTE) mismatches. The TiC has a lower CTE as compared to tool steel. If the TiC coating were to adhere to the tool steel, tensile stresses would be generated in it when the sample was heated up to 1200 °C. These tensile stresses could cause pre-existing flaws in the coating to propagate, resulting in cracks in the coating which would allow penetration of the infiltrant. If the coating were not adherent, then it would not crack and result in penetration. This is consistent with the experimental observations in the last section.

8 Conclusion and Future Work

8.1 Conclusion

An effort was initially made to make the 420/bronze system re-hardenable by introducing an annealing and quenching treatment after infiltration. The results indicated limited re-hardenability of the 420/bronze along with a 0.2 % expansion that was observed during the heat treatment. This resulted in an overall consensus that the 420/bronze was not particularly suited for re-hardening purposes and hence a new system needed to be developed.

An effort was made to optimize the printing and post processing parameters for a new system comprised of Mo powder and a Cu-Ni-Mn age hardenable infiltrant. The post processing cycle comprised debinding/sintering, infiltration and age hardening. The number of steps in the post processing of Mo/Cu-Ni-Mn are reduced compared with those for the 420/bronze system. The sintering and debinding steps are combined into one step and there is also no annealing treatment in the newly developed post processing cycle for the Mo/Cu-Ni-Mn system. This simplifies the post processing operation.

The printing of acrysol binder into 62 μm Mo powder was very successful. The parts showed good surface finish and edge definition. The printing parameters are listed in Appendix 2. On the other hand, the printing of 30 μm Mo powder was not as successful due to poor flowability of the powder and the balling phenomenon, which was observed during the printing. The 30 μm Mo powder may have shown poor flowability due to the presence of fines. The balling might be eliminated by decreasing the droplet spacing or reducing the droplet frequency. Hence, a decision was made to develop a process for making tools with the 62 μm Mo powder.

A debinding and sintering treatment was developed for the 62 μm Mo powder. The details of the treatment are included in Appendix 3. Several parts have been processed using this treatment. The dimensional shrinkage during sintering was about 0.3 %. This is a lot less than that obtained in the 420/bronze system, which was about 2%. The smaller shrinkage is associated with a smaller variability in shrinkage. Although the sintering strength obtained is good enough to withstand infiltration, the part is still very vulnerable to damage and needs to be handled very carefully. An improvement in the strength would be desirable.

Theoretical studies on the sintering of Mo have indicated that the neck size ratio and shrinkage are very sensitive to the sintering temperature and the particle size. Hence in order to obtain better sintering strength, the sintering should be carried out at a higher temperature or a smaller powder size should be used. Another potential advantage would be the sintering time could also be cut down, thus reducing the cycle time for the operation.

A theoretical model was used to study the sintering of Mo and predict shrinkage accurately. The details of this study are included in Appendix 4. The shrinkage values predicted by the modeling effort matched those observed experimentally. The debinding treatment was found to leave an acrysol residue on the Mo particles. It was proposed from experimental findings that the acrysol residue activates the surface diffusion in the sintering of Mo, resulting in a larger neck size and a better strength with low shrinkage.

The infiltration of the Mo skeleton with a 60Cu-20Ni-20Mn infiltrant was also studied extensively. An infiltration treatment was developed and is detailed in Appendix 3. The optimal infiltration treatment is for 45 minutes at 1200 °C in a hydrogen atmosphere. Several parts including a tool with conformal cooling channels have been infiltrated successfully. The wetting behavior appears to improve with increasing temperature or a reducing atmosphere. This is consistent with observations by other researchers. The wetting is very good under the optimal infiltration conditions. "Thermo-Calc" studies have shown that there is little solubility of Mo in 60Cu-20Ni-20Mn up to 1200°C. At

higher temperatures the solubility of Mo in Cu-Ni-Mn increases. This has been verified experimentally. Microprobe studies show no Mo in the solidified infiltrant. Hence, the erosion observed in the 420/bronze system is absent in the new Mo/Cu-Ni-Mn system. As a result of the small interaction, there was no swelling observed during infiltration in the Mo/Cu-Ni-Mn system.

The porosity control during infiltration is also significantly improved relative to the 420/bronze system. The porosity in the Mo/Cu-Ni-Mn infiltrant has been observed to be less than 1%. One disturbing observation was the gas porosity that was observed under the excess infiltrant around the stilt. This was found to occur due to a reaction between the Cu-Ni-Mn infiltrant and the alumina plate. Despite the excellent wetting between the infiltrant and the skeleton, the tool still leaked i.e. there was continous porosity between the cooling channels and the working surface. In order to test wether the leaking was due to gas porosity in the tool, another tool was infiltrated in vacuum. This tool also leaked suggesting that the solidification shrinkage of the infiltrant might be causing the leaking. Possible solutions in order to prevent leaking are directional solidification of the infiltrant and a smaller Mo powder size and printing of a stilt on to the tool.

No slumping of the part was observed during the infiltration. A small shrinkage of 0.2 % was also observed. This might be due to a liquid phase sintering effect that might be occurring. The Mo/Cu-Ni-Mn part showed very little oxidation during the infiltration. The tendency of Mo to oxidize is the same as Fe and a lot less than that of Cr in 420 stainless steel. The only element that has a very high tendency to oxidize is the Mn in the infiltrant. The furnace requirements should be designed to prevent the oxidation of Mn.

The Mo particles at the edge of the Mo/Cu-Ni-Mn appeared to have broken down. This might be due to an increased solubility of Mo in the liquid Cu-Ni-Mn due to higher temperatures at the tool surfaces, or possibly due to a hydrogen interaction.

After studying the Cu-Ni-Mn ternary, the solidification range of the 60Cu-20Ni-20Mn infiltrant was determined to be 1040 °C - 1060 °C. For the 60Cu-20Ni-20Mn alloy, the

critical temperature below which the NiMn precipitate is stable was found to be 510 °C. Earlier work has indicated that the optimal age hardening treatment for 60Cu-20Ni-20Mn is a solution treatment at 650 °C for 1 hour followed by an aging treatment at 350 °C-450 °C. Due to the small size of the precipitate (~1 μm), the elemental composition of the precipitate could not be determined for our specimens. However previous work has indicated these precipitates are an equiatomic ordered NiMn phase with an $L1_0$ structure. The hardness of the Cu-Ni-Mn was observed to increase with time, initially at a faster rate but it gradually became smaller. Very little hardening has been known to be observed after an aging time of 24 hours. An increase in the Ni and Mn content has been known to increase the initial hardening rate but it does not affect the level of hardness obtained at high aging times. The maximum hardness obtained from the optimal age hardening treatment was just below 50 Rc.

Experimental work with an alloy of composition 56at.% Cu, 22at.% Ni and 22 at.% indicated hardness levels that matched work performed by earlier researchers. An optimal age hardening treatment was developed which is given in detail in Appendix 3. The treatment consisted of solution at 650 °C for 1 hour and an age hardening treatment at 450 °C for 48 hours in a forming gas atmosphere. The hardness obtained in the infiltrant from this treatment is 47 Rc. Very slight oxidation of the part was observed during the age hardening treatment.

Part distortion resulting from the age hardening treatment is negligible. This is due to the non-aggressive nature of the age hardening treatment. This is not so for the quenching treatment in 420/bronze. Another advantage with the Mo/Cu-Ni-Mn system is that both the powder particle and the infiltrant are hard. This is not true for the 420/bronze system. The macro-hardness for the hardened Mo/Cu-Ni-Mn system is similar to that in the 420/bronze system.

The main concern with the Mo/Cu-Ni-Mn system is the poor electro-discharge machining (EDM) characteristics. This is primarily due to the high melting point of Mo. Alternative powders were considered. The two other elements that wetted Cu-Ni-Mn but did not

dissolve in it were W and Ta. Unfortunately, both these elements have a melting point higher than Mo, which would not help the EDM characteristics of a composite tool.

Another approach is to use a hardenable lower melting powder like 420 with Cu-Ni-Mn infiltrant. Unfortunately 420 was found to dissolve in the infiltrant. A diffusion barrier could be used to prevent the interaction. An attempt was made to coat the tool steel with TiC and infiltrate with 56Cu-22Ni-22Mn. The infiltrant appeared to penetrate the coating and react with the steel below. After looking carefully at diffusion data, it was decided that the penetration occurred mainly due to flaws in the coating rather than diffusion through the coating.

The thermal conductivity of the tool is very important since heat transfer from the tool surface to the cooling channels is very important. The thermal conductivity of Mo is about 10 times that of 420 steel. On the other hand the thermal conductivity of the Cu-Ni-Mn alloy is at least 10 times worse than that of Cu-10Sn. Hence the expected conductivity for the entire composite is expected to be similar for both materials systems. The electrical conductivity of Cu-Ni-Mn has been observed to improve drastically after the aging treatment. If this behavior translates to the thermal conductivity, it could significantly improve for the composite.

Table 8-1 compares the new Mo/Cu-Ni-Mn system with the original 420/bronze system.

	420/Cu-10Sn	Mo/56Cu-22Ni-22Mn
Dimensional Tolerance	> 1 %	< 0.6 % shrinkage
Porosity	leakage occurred, < 1% porosity	slight leakage, < 1 % porosity
Erosion	Considerable solubility of Fe in Cu-10Sn	Very little solubility of Mo in 56Cu-22Ni-22Mn
Interdiffusion	Greater due to smaller melting point difference	Smaller due to greater melting point difference
Hardness	Macro ~ 22 Rc 420 : 60 Rc, Cu-10Sn : 80 Rb	Macro ~ 100 Rb or 20 Rc, Mo : 95 Rb, Cu-Ni-Mn~ 47 Rc
Oxidation	Cr oxidation, $P_{O2} \sim 10^{-18}$ atm	Mn is a problem, $P_{O2} \sim 10^{-30}$ atm
Galvanic Corrosion	Galvanic corrosion possible	Galvanic corrosion possible
Thermal Conductivity	420 : 0.15 W/cm K 420/Cu-10Sn : Fair	Mo : 1.38 W/cm K Mo/Cu-Ni-Mn : Fair

Table 8-1 : Comparison between the 420/bronze and Mo/56Cu-22Ni-22Mn systems.

8.2 Future work

There is a lot of scope for future work in several areas in order to develop an age hardenable system. With regards to the Mo/Cu-Ni-Mn system, additional work could be performed in several areas. The printing of finer Mo powders (30 μm) could be pursued. This would be a significant breakthrough because it will improve as-sintered strength. Another way to improve the sintering strength would be to use a furnace capable of temperatures higher than 1200 °C. Going to higner sintering temperatures could also reduce the sintering times.

The leaking of the tools is an issue that has to be addressed. The directional solidification of the Cu-Ni-Mn infiltrant could be looked into. Another solution might be to use a finer powder size.

The composition of the age hardening alloy could also be varied. By using higher amounts of Ni and Mn, the aging time might be able to be reduced while retaining the same hardness. Some TEM work could also be done to learn more about the nature of the age hardening reaction in Cu-Ni-Mn alloys. The effect of precipitation on the thermal conductivity of the composite could also be studied.

The work on TiC coatings on tool steel looks very promising. Other coatings could be tried on the tool steel. These coatings could be ceramic or metallic. If a successful coating is found, it will make the 420/Cu-Ni-Mn system very promising. There would still however be issues pertaining to sintering strength, wetting, porosity etc.

Appendix 1 The post infiltration heat treatment of 420/bronze

1. Post processing procedures :

1.1 Annealing :

(a) ramp up at 5 °C/min to 800 °C.
(b) hold 90 minutes at 800 °C. (times depends on the size of the part [11])
(c) ramp down at 1 °C/min to 250 °C.
(d) ramp down at 2 °C/min to RT.

1.2 Normalizing and Quenching :

(a) ramp up at 10 °C/min to 880 °C.
(b) hold for 90 minutes at 880 °C. (time is a function of the size of the part)
(c) furnace cool from 880 °C to RT.

Appendix 2 Printing parameters for the Mo (62 μm) powder

Printing Parameters :

Fast Axis Speed	1.5 m/sec
Binder Flow Rate	1.15 cc/min
Layer Thickness	170 μm
Row Spacing	202 μm
Packing Fraction	60%
Saturation	97 %

The parameters were selected in order to obtain a binder saturation of 97%. The 62 μm Mo powder was printed successfully with acrysol binder using the above parameters. The printed part could be easily removed from the loose powder bed. The surface finish and edge definition of the part were very good. After the printing of the tools with cooling channels, the powder could be removed easily from the cooling channels.

Appendix 3 Post processing parameters and procedures for Mo/56Cu-22Ni-22Mn

1. Post processing parameters.

1.1 Debinding and Sintering. (forming gas atmosphere,30 SCFH, MRF high temp. furnace)

(a) ramp up 5 °C/min to 200 °C
(b) hold 30 min at 200 °C.
(c) ramp up 5 °C/min to 500 °C.
(d) hold 30 min at 500 °C
(e) ramp up 5 °C/min to 1200 °C.
(f) hold 12 hours at 1200 °C.
(g) ramp down at 5 °C/min to room temperature (RT).

1.2 Infiltration. (hydrogen atmosphere, 10 SCFH, MRF high temp. furnace)

(a) ramp up at 10 °C/min to 1200 °C.
(b) hold 45 min at 1200 °C.
(c) ramp down at 10 °C/min to RT.

1.3 Age hardening.(forming gas atmosphere 2 SCFH, Adams box furnace)

(a) ramp up at 20 °C/min to 650 °C.
(b) hold 1 hour at 650 °C.
(c) ramp down at 10 °C/min to 450 °C
(d) hold 48 hours at 450 °C
(e) ramp down at 10 °C/min to RT.

2. Post processing procedures.

2.1 Preparation for debinding and sintering.

(a) check quality of printed part.
(b) make sure all loose powder is cleaned out.
(c) measure dimensions on at least 12 points on the part.
(d) select a graphite crucible of the appropriate dimension and place an alumina substrate at the bottom of the crucible.
(e) place the part on the alumina substrate.
(f) sieve the zirconia powder with a 75 μ sieve.

(g) pour the zirconia powder into the crucible and cover the entire sample.
(h) shake or vibrate the crucible to obtain a dense or uniform packing.
(i) place the crucible at the center of the MRF high temperature furnace.
(j) perform the run after setting up the furnace.

2.2 Preparation for infiltration.

(a) clean the part after sintering.
(b) measure dimensions along the same 12 points.
(c) make a stilt of sintered Mo powder. (1200 °C for 12 hours)
(d) paint the crucible on the inside with BN.
(e) place the stilt at the center of the crucible after the BN dries. (do not place an alumina sheet at the bottom)
(f) place the sample on top of the stilt.
(g) calculate the required amount of Cu-Ni-Mn infiltrant from the density and volume required.
(h) place the Cu-Ni-Mn infiltrant chunks around the stilt.
(i) place a stainless steel tray at the bottom of the MRF high temperature furnace for protection incase the crucible breaks.
(j) place the graphite crucible on the stainless steel tray with a separation of an alumina blanket.
(k) cover the graphite crucible with a graphite substrate to protect against any evaporation or deposition.
(l) set up the program and perform the run.
(m) wait for 2 hours after the furnace thermocouple reads RT to allow for the proper cooling of the part.

2.3 Preparation for age hardening.

(a) cut the part from its stilt and machine the bottom surface smooth.
(b) place the part in a furnace designed for long runs.
(c) make sure to check on the forming gas supply.
(d) set up the furnace and perform the run.

Appendix 4 Theoretical prediction of shrinkage during sintering

3.1 Background and Method.

The sintering can be divided into three stages based upon the amount of neck formation and pore characteristics. An initial stage, an intermediate stage, and a final stage. The factor used to separate these stages, is the neck to particle size ratio. (Figure 4-1) Chapter 4 dealt with the primarily the initial stage of sintering.

The initial stage is associated by interconnecting pores and a neck size ratio of less than 0.3, while the intermediate and final stages are characterized by cylindrical and circular pore structures with neck size ratio increasing.

In the initial stage, there are several diffusion mechanisms acting simultaneously. The contribution from these mechanisms, surface diffusion, volume diffusion, grain boundary diffusion etc. can be expressed as a sum of terms that contribute to the neck size ratio:

$$\Sigma(X/D)= (X/D)_{\text{surface diffusion}} + (X/D)_{\text{volume diffusion}} + \ldots\ldots$$

The above terms vary are a function of the holding time (t), particle radius (R), and mechanism specific exponents (m,n) :

$$(X/R)^n = Bt/R^m$$

The parameter (B), depends on the diffusivity of the sintering mechanism under consideration (which varies exponentially with temperature), and various other constants relating to the mechanism. Using surface diffusion as an example, the parameter for surface diffusion (B_s) and the associated diffusion constant (D_s) would vary as shown below,

$$B_s= 56D_s\gamma\Omega^{4/3}kT$$

$$D_s=A_s \exp(-Q_s/RT)$$

Where γ, Ω_s, A_s, Q_s are the surface energy, atomic volume, frequency factor and activation energy for surface diffusion, respectively. The symbols R, K, T refer to the gas constant, Boltzman's constant and the temperature respectively.

Once the individual contributions to the neck growth have been accounted for and combined (typically in a spreadsheet), the next task is to predict the shrinkage. German

[15] has presented an approximate relationship between the neck size ratio and the shrinkage :

$\Delta L/L^{o} = (X/R)^{2}$

This relationship can then be used as a guide in determining the sintering times and temperatures.

A list of the relations that can be used for the different sintering mechanisms is presented in the following table. [15]

Sintering Mechanisms	Diffusion constant	B	n	m
Surface Diffusion	$D_s=A_s \exp(-Q_s/RT)$	$B_s= 56D_s\gamma\Omega^{4/3}kT$	7	4
Volume Diffusion	$D_v=A_v \exp(-Q_v/RT)$	$B_v= 80D_v\gamma\Omega/kT$	5	3
Grain Boundary Diffusion	$D_{gb}=A_{gb} \exp(-Q_{gb}/RT)$	$B_{gb}= 56D_{gb}E_{\gamma\beta}\Omega/kT$	6	4
Plastic Diffusion	$D_p=A_p \exp(-Q_p/RT)$	$B_p= 9\pi\gamma bD_v\Omega/kT$	2	1

Material property data used to generate the sintering and shrinkage plots in Chapter 4 is also listed in in the following table.

Name	Symbol	Value	Units
Atomic Volume	Ω	1.1249E-29	m^3
Burgers Vector	b		m
Density	ρ	10200	Kg/m^3
Shear Modulus at 300K	G		Mn/m^3
Temperature dependence of shear modulus			
Melting Temperature	T_m	2883	K
Grain Boundary Energy	E_{gb}		J/m^3
Surface Energy	γ_s	2.2	J/m^2
Pre-exponential term for volume diffusion	A_v	0.00005	m^2/s
Activation energy for volume diffusion	Q_v	418000	J/mole
Pre-exponential term for grain boundary diffusion	A_{gb}	6E-14	m^3/sex
Activation energy for grain	Q_{gb}	263000	J/mole

boundary diffusion			
Pre-exponential term for surface diffusion	A_s	10	m^3/sec
Activation energy for surface diffusion	Q_s	241000	J/mole

Appendix 5 Infiltration of liquid Cu-Ni-Mn into a Mo skeleton.

The wetting between the Cu-Ni-Mn infiltrant and the Mo skeleton has been found to be very good at 1200 °C in a reducing atmosphere of hydrogen. At the same time the reaction between the infiltrant and the skeleton is minimal. This makes it an ideal combination of infiltrant and skeleton for infiltration purposes. An approximate calculation was made in order to estimate the maximum height to which the infiltrant could climb within the porous Mo skeleton as a result of the capillary forces. This height is represented by the following equation:

$$h= (2\gamma\cos\theta)/(r\rho g)$$

where: 'h' is the height that the liquid Cu-Ni-Mn can rise up into the Mo skeleton.
'γ' is the surface tension of liquid Cu-Ni-Mn = 1 N/m
'r' is the radius of the Mo powder particle = 30 μm
'ρ' is the density of Cu-Ni-Mn = 8635 kg/m^3
'g' is the acceleration due to gravity = 9.8 m/sec^2

Plugging into the above equation: h~ 1m

This is a conservative height because the actual surface tension of Cu-Ni-Mn is expected to be greater than 1 N/m. This infiltration height for the tools is well within a meter and hence capillarity is not expected to be a problem.

Appendix 6 Diffusion in Mo

Diffusion data was obtained for bulk diffusion and surface diffusion in Mo from the "Diffusivity Data Series Handbook". The following data was obtained :

Diffusion in Mo :

Diffusion Mechanism	Element	Temperature (°C)	Diffusivity (cm^2/sec)
Surface	Mo	1600	10^{-7}
Bulk	C	1500	10^{-6}
Bulk	Ni	1350	10^{-12}
Bulk	K (tracer)	1100	10^{-13}

Mo surface diffusion has been known to employ grain boundary grooving techniques. This has been experimentally observed. From the above data it can be concluded that at 1200 °C the diffusion of other metal atoms in Mo is negligible. The surface of diffusion of Mo at 1200 °C of Mo appears to be faster than the diffusion of other foreign atoms in Mo.

Using the data in Appendix 4, the surface, volume and grain boundary diffusivities of Mo are calculated at 1200 °C.

$D_{surface} = A_{surface}\exp(-Q_{surface}/RT) = 10\exp(-241000/(8.314*1473)) = 2.84 \times 10^{-8}$ cm^2/sec.

$D_{gb} = A_{gb}\exp(-Q_{gb}/RT) = 6*10^{-14}\exp(-263000/(8.314*1473)) = 7.1 \times 10^{-10}$ cm^2/sec.

$D_{volume} = A_{volume}\exp(-Q_{volume}/RT) = 5*10^{-5}\exp(-418000/(8.314*1473)) = 2.83 \times 10^{-23}$ cm^2/sec.

From the diffusivity data it is apparent that the surface diffusion dominates.

Appendix 7 Diffusion through TiC

Data for bulk diffusion through TiC was obtained from the "Diffusivity Data Series" handbooks. Bulk diffusion can occur via interstitials or vacancies.

Mechanism	Element	Temperature	Diffusivity (cm^2/sec)
Bulk (Vacancy)	C	1200 °C	10^{-12}
Bulk (Vacancy)	Ti	1200 °C	10^{-16}

The diffusion of Ti through TiC is 10^4 times slower than C through TiC. The diffusion of Ti and C atoms through TiC has been found to be vacancy assisted. Diffusivity of Ti and C increases as the porosity increases The diffusion of other metal atoms through TiC is expected to be similar to that of Ti.

As described in Chapter 7, TiC coated tool steel samples were immersed in a Cu-Ni-Mn infiltrant at 1200 oC for 1 hour. The infiltrant appeared to have penetrated the coating and dissolved the tool steel.

A theoretical calculation was done after careful study of the microstructure in Figure 7-. An approximate estimation of the diffusivity of Cu, Ni and Mn atoms through TiC was made after looking at the penetration of the infiltrant through the TiC coating.

The following data was obtained from the microstucture :

The depth of penetration of the coating, 'L'=0.02 cm
The time for which diffusion would be occurring (time of immersion) , 't' = 1 hour
The thickness of the coating, 'd'= 3 μm.
Area of cross section over which infiltration occurs : A cm^2.

According to Fick's first law : $J=-D(dc/dx)$
One dimensional steady state solution : $J=-D(\Delta c/\Delta x)$
Assume one side of the coating is pure Cu-Ni-Mn with C_o moles/cm^3 and the other side has no infiltrant.

Then $\Delta c = C_o - 0 = C_o$.

$\Delta x = d$

Therefore $J = -D(C_o/d)$

Also $J = (LC_o/t)$

Equating the two expressions for 'J' the expression for diffusivity is $D = dL/t$.

Plugging in the values for L, d and t the value for $D = 10^{-9}$ cm^2/sec.
Hence, if the Cu, Ni and Mn atoms diffused through the TiC layer, the minimum diffusivity required would be 10^{-9} cm^2/sec. The diffusion data from literature states that the diffusivities of metal atoms through TiC are a lot lower, around $10^{-16} cm^2/sec$ at 1200 °C. This suggests that the penetration of the infiltrant was not a result of diffusion through the coating. The reason for the penetration is more likely flaws that exist in the coating through which the coating penetrates.

One of the reasons for the flaws might have to do with mismatch in the thermal expansion of the coating and the steel. The coating thickness (3μm) is high enough for significant stresses to be generated in it as a result of mismatch in the CTE (coeff. of thermal expansion). The CTE for TiC is much lower than that of the tool steel. This will cause a greater expansion in the tool steel due to a CTE mismatch, during the ramp up to 1200 °C. Hence, a tensile stress will be generated in the coating which will result in the propagation of any pre-existing flaws in the coating.

Another reason might have to do with the coating technology and adherence of the coating at elevated temperatures.

Appendix 8 Electrochemical and thermodynamical data

The following data gives the reduction potential for many elements [22].

Reaction	E^o (V)
$K^+ + e = K$	-2.931
$Na^+ + e = Na$	-2.71
$Zn^{+2} + 2e = Zn$	-0.744
$Fe^{+2} + 2e = Fe$	-0.447
$Ni^{+2} + 2e = Ni$	-0.250
$Mo^{+3} + 3e = Mo$	-0.2
$2H^+ + 2e = H_2$	0
$Cu^{+2} + 2e = Cu$	+0.342

The Mo is less active than Fe and hence has a greater tendency to remain elemental form. Thus it is more corrosion resistant than Fe. It has a tendency to be attacked by Cu^{+2} ions.

The following data gives the Gibbs free energy of formation for several metal oxides.

$2[Cu] + O_2 = Cu_2O$ ΔG^o (kJ/mole) = -339.762+0.14886T

$2\{Cu\} + O_2 = Cu_2O$ ΔG^o (kJ/mole) = -380.482+0.177T

$2[Ni] + O_2 = 2NiO$ ΔG^o (kJ/mole) = -471.938+0.17216T

$2[Fe] + O_2 = 2FeO$ ΔG^o (kJ/mole) = -538.986+0.1254T

$[Mo] + O_2 = MoO_2$ ΔG^o (kJ/mole) = -581.245+0.17281T

$2[Mn] + O_2 = 2MnO$ ΔG^o (kJ/mole) = -769.704+0.14664T

$4/3[Al] + O_2 = 2/3Al_2O_3$ ΔG^o (kJ/mole) = -1105.785+0.210T

An Ellingham diagram was constructed with the above data and is included in Figure 5-9. The most important finding is the similar oxidation tendency for Fe and Mo. The element in Mo/Cu-Ni-Mn which has the highest tendency to oxidize is Mn. Cu and Ni have a much smaller tendency to oxidize versus Mn. The oxidation tendency for Mo lies between Mn and Cu.

Appendix 9 Shrinkage during the sintering and infiltration of tools for Motorola

The following table shows the shrinkages that were obtained across several dimensions during the processing of the tools for Motorola. The shrinkage was anisotropic. The sintering shrinkage obtained for the tools was less than that obtained for the coupons during the sintering experiments described in section 4.4.2. On the other hand, the infiltration shrinkage was higher than that observed in the coupons during the infiltration experiments in section 5.3.1

Tool #1					
	As printed (inches)	**Sintered (inches)**	**Infiltrated (inches)**	**Sintering shrinkage**	**Infiltration shrinkage**
Length	4.069	4.0598	4.03925	0.22%	0.50%
Width	3.046	3.04125	3.026	0.17%	0.50%
Thickness	1.173	1.1716	1.164	0.10%	0.65%
Tool #2					
	As printed (inches)	**Sintered (inches)**	**Infiltrated (inches)**	**Sintering shrinkage**	**Infiltration shrinkage**
Length	4.071	4.06088	4.04225	0.25%	0.46%
Width	3.0475	3.042	3.0261	0.18%	0.52%
Thickness	1.0175	1.0155	1.0116	0.02%	0.38%

Appendix 10 Shrinkage during the sintering of Mo.

T=1200 °C t=4 hours						
Pure Mo (30 μm)				Pure Mo (30 μm) + acrysol		
Before	After	Shrinkage (%)		Before	After	Shrinkage (%)
23.044	22.988	0.24		22.853	22.749	0.46
23.747	23.617	0.55		20.971	20.867	0.50
24.451	24.328	0.50		20.721	20.619	0.49
24.47	24.361	0.45		21.095	20.988	0.51
Pure Mo (62 μm)				Pure Mo (62 μm) + acrysol		
Before	After	Shrinkage (%)		Before	After	Shrinkage (%)
23.739	23.702	0.16		24.437	24.368	0.28
23.983	23.953	0.13		24.121	24.059	0.26
24.731	24.701	0.12		24.28	24.222	0.24
24.042	24.012	0.12		24.861	24.822	0.16
T=1200 °C t=12 hours						
Pure Mo (30 μm)				Pure Mo (30 μm) + acrysol		
Before	After	Shrinkage (%)		Before	After	Shrinkage (%)
23.233	23.107	0.54		22.02	21.854	0.75
23.432	23.277	0.66		17.877	17.756	0.68
23.751	23.604	0.62		19.109	18.979	0.68
24.43	24.308	0.50		19.507	19.365	0.73
Pure Mo (62 μm)				Pure Mo (62 μm) + acrysol		
Before	After	Shrinkage (%)		Before	After	Shrinkage (%)
23.231	23.165	0.28		16.527	16.465	0.38
23.783	23.738	0.19		14.592	14.538	0.37
24.543	24.495	0.20		20.4	20.333	0.33
24.987	24.943	0.18		20.045	19.996	0.24

Bibliography

1. Sachs, E., Haggerty, J., Williams, P., and Cima, M., *U.S. Patent*, 5204055, 1993.
2. Sachs, E., *et al.* "Injection Molding Tooling by Three Dimensional Printing,"*Rapid Prototyping and Manufacturing '96*, Dearborn, MI, Rapid Prototyping Association of SME, 1996.
3. Sachs, E., "Tooling by 3D Printing; Hardness, Dimensional Control, Surface Finish and Conformal Cooling," *Rapid Prototyping and Manufacturing '97*, Dearborn, MI, Rapid Prototyping Association of SME, 1997.
4. Guo, H., "Alloy Design for Three Dimensional Printing of Hardenable Tool Materials," *Ph.D. Thesis*, Massachusetts Institute of Technology, Cambridge, p.1-38, 1998.
5. Michaels, S., "Production of Metal Parts Using the Three Dimensional Printing Process," *M.S. Thesis*, Massachusetts Institute of Technology, Cambridge, p25-35, 1989.
6. Winchell, P., and Cohen, M., *Trans. ASM*, Vol 55, p.347, 1962.
7. Roberts, C., *Trans. AIME*, Vol 197, p.203, 1953.
8. Lorenz, A., "Economical Furnace Processing for Three Dimensional Printed Metal Parts", *M.S. Thesis*, Massachusetts Institute of Technology, Cambridge, p.32-33, 1998.
9. Morrow, F., "Testing and Inspection of Casting Defects," Casting, Vol. 15, *ASM Handbook*, Ohio: American Society for Metals, 1988, p.544-561.
10. *Metals Handbook*, Vol.1 and Vol.2, 10th edition, ASM, 1992.
11. *Heat Treater's Guide*, 2nd edition, ASM, p.775-776, 1996.
12. Baker, P., "Three Dimensional Printing of Fine Metal Powders", *M.S. Thesis*, Massachusetts Institute of Technology, Cambridge, p.20-30, 1997.
13. Oton, A., "High Density Bimodal Parts by Three Dimensional Printing," *M.S. Thesis*, Massachusetts Institute of Technology, Cambridge, p.88-89, 1998.
14. Kingery, W., *Introduction to Ceramics*, Wiley, p.475-480, 1976.
15. German, R., *Powder Metallurgy Science*, Metal Powder Industries Federation, Princeton, NJ, 1984.
16. Young, W., "Molybdenum Sintering and the Molybdenum-Oxygen-Carbon System," *J. of the Less-Common Metals*, Vol.32, p.321-330, 1973.
17. Yoo, H., "Reactive Binders for Metal Parts Produced by Three Dimensional Printing," *M.S. Thesis*, Massachusetts Institute of Technology, Cambridge, p.16-19, 1997.
18. Handbook of Metal, "Phase Diagrams", 10th edition, ASM, 1992.
19. Yupko, V., "Wetting of Molybdenum and Lanthanum Hexaboride by Alloys Cu-Bi, Cu-Sb in Various Media," Institute of Materials Science, Academy of Sciences of the Ukrainian SSR. Translated from *Poroshkovaya Metallurgiya*, Vol.11, p.64-69, November, 1986. Original article submitted January 6, 1985.
20. Parravano, N., "The Ternary Alloy of Ni-Mn-Cu," *Gazz. Chim.* Ital., Vol.42, p.385-394, 1912, in Italian.

21. Hansen, M., *Constitution of Binary Alloys*, 2nd edition, McGraw Hill.

22. Lide, D., *Handook of Chemistry and Physics*, Student Edition, CRC Press, p.5-72, p.4-119.
23. Jones, A., *Principles and Prevention of Corrosion*, 2nd edition, Prentice Hall, p.519-523.
24. Dieter, G., *Mechanical Metallurgy*, SI Metric Edition, McGraw Hill, p.212-215, 1989.
25. Henry, C., "Estimation of the $L1_o$ NiMn phase region in the NiMn system", *MIT Report*, December, p.1-40, 1997.
26. Chang, B., "Investigation of Ternary Copper-Nickel-Manganese Alloys",*Vyssh. Ucheb. Zaved.*, Tsvet. Met.,Vol.5, p.107-115, 1958, in Russian.
27. Tsiuplakis K. and Kneller E., "The Constitutional Diagram Mn-Ni", *Z. Metallk.*, Vol.60, p.433-438, 1969, in German.
28. Rolland, J. and Whitwham, D.," Critical Temperatures of Cu-Ni-Mn Alloys:, *Mem. Sci. Rev. Met.*, Vol.67, p.607-614, 1970, in French.
29. Dean, R., Long, J., Graham, T., and Mathews, C., "Age Hardening Cu-Mn-Ni Alloys", *Trans. ASM*, Vol.34, 1945.

THESIS PROCESSING SLIP

FIXED FIELD: ill. _____ name _____

index _____ biblio _____

► **COPIES:** (Archives) Aero Dewey Barker Hum

Lindgren Music Rotch (Science) Sche-Plough

TITLE VARIES: ► ☐ _____

_____

_____

NAME VARIES: ► ☐ _____

_____

IMPRINT: **(COPYRIGHT)** _____

_____

► **COLLATION:** _____

_____

► **ADD: DEGREE:** _____ ► **DEPT.:** _____

► **ADD: DEGREE:** _____ ► **DEPT.:** _____

SUPERVISORS: _____

_____

NOTES:

_____ cat'r: _____ date:

page:

► **DEPT:** [illegible]

► **YEAR:** [illegible] ► **DEGREE:** [illegible]

► **NAME:** [illegible]

_____